Microvoiding and Constitutive Damage Modeling with Artificial Neural Networks

Ning Li, Huck Beng Chew*

Department of Aerospace Engineering, University of Illinois at Urbana-Champaign, Urbana IL 61801, USA

*Author to whom all correspondence should be addressed. Email: hbchew@illinois.edu

Abstract

Continuum models of porous media have revolutionized computational fracture mechanics for traditional ductile materials, but the inherent assumptions have limited generalizability to other target materials or loading conditions. Here, we adopt a series of artificial neural networks (ANNs) to predict both the microscopic voiding characteristics (void shape, porosity) and macroscopic stress-strain constitutive response of porous elasto-plastic materials under various deformation states. We train the ANNs on a dataset generated from finite element models of 3D representative volume elements (RVEs), each containing a discrete spherical void, subjected to combinations of loading states. Results show that the data-driven model is capable of interpolative predictions as well as some levels of extrapolative predictions across a wide range of initial porosities (0-20%) and loading states outside of the training dataset, even at high deformation strains which induce extensive material softening and void growth. Through transfer learning, we further demonstrate that the ANNs, originally trained on a specific porous material dataset, can be readily adapted to other porous materials with substantially different properties through a significantly reduced training dataset. We discuss the implications of this machine learning approach vis-à-vis the extensively-developed Gurson model for porous material damage and failure predictions.

Keywords: Machine learning, Gurson model, neural network, void growth, void shape, porosity

1. Introduction

Fracture and failure of a material is generally preceded by the development of cracks at stress hot-spots, which originate from the inherent microstructural heterogeneity or inhomogeneous defect distribution within the material (Chan, 2010; Abuzaid et al., 2013; VanSickle et al., 2020). In conventional metals and alloys, the dimpled ductile fracture surface is caused by the growth and coalescence of ~2-12 μm microvoids, which nucleate from inclusions and second-phase particles within the metal matrix (Stone et al., 1985; Faleskog & Shih, 1997). In addition to these ~2-12 μm background microvoids, incomplete laser melting of the powder particles or gas entrapment bubbles in additively-manufactured metals results in the formation of larger ~30-60 μm processing defects (Panwisawas et al., 2017; Snow et al., 2020) to create a two-scale porosity microstructure (Cui et al., 2020; Muro-Barrios et al., 2022). The resulting macroscopic ductile fracture response of additively-manufactured metals can significantly differ from their conventional counterparts because of the heterogeneous distributions of these larger processing microvoids (Foehring et al., 2018; VanSickle et al., 2020).

The micromechanics modeling of materials facilitates bridging of the micro-to-macro scales by homogenizing the underlying mechanistic processes of material separation (e.g., void growth and coalescence) within the narrow fracture process zone ahead of a crack into equivalent crack-tip constitutive laws (Hutchinson & Evans, 2000). In the cohesive zone approach, one homogenizes the complicated micromechanical failure mechanisms within the fracture process zone ahead of a physical crack into an equivalent traction-separation constitutive relation (Dugdale, 1960; Barenblatt, 1962; Tvergaard and Hutchinson, 1992). Often, a functional form of this traction-separation relation (e.g., trapezoidal, bilinear, exponential) is assumed a-priori, and parameters, such as the peak cohesive traction and the cohesive energy are fitted to experimental

data (Tvergaard & Hutchinson, 1992; Guo et al., 1999; Williams & Hadavinia, 2002; Valoroso & Fedele, 2010), rendering these cohesive zone models to be more phenomenological in nature. Recent studies, however, have shown that the exact functional form of the cohesive zone law represents key physical fracture processes (Chew et al., 2009; Hong et al., 2009; Chew, 2014; Tran & Chew, 2022). This has motivated the development of inverse approaches to reconstruct the exact functional form of the cohesive zone law from the remote strain fields surrounding a cohesive crack-tip (Kim et al., 2012; Chew, 2013; Tran et al., 2022).

An alternative to the cohesive zone law approach for ductile materials is to provide a detailed representation of the fracture process zone by directly simulating the nucleation, growth, and coalescence of voids, viz. row(s) of void-containing computational cell elements ahead of the crack. These computational cell elements are governed by a micromechanical damage model – the Gurson model and its variants – that accounts for the constitutive response of void growth in a representative volume element (RVE), through a plastic yield function that has porosity has a damage parameter, and a damage evolution law (Gurson, 1977; Tvergaard, 1981). The porosity gives rise to an apparent dilatancy and pressure sensitivity of the macroscopic plastic deformations, and allows for modeling of material softening and the loss of stress-carrying capacity before failure. This computational cell element approach is capable of reproducing the details of damage dissipation within the process zone to predict monotonic or even fatigue crack growth in a wide variety of material systems, including conventional metal alloys, polymeric materials, and even more recently, a two-scale porosity media resembling additively-manufactured metals (Xia & Shih, 1995; Chew et al., 2005; Tekoglu & Nielsen, 2019; Cui et al., 2020; Muro-Barrios et al., 2022). Nevertheless, these macroscopic failure predictions are limited by the inherent assumptions of the micromechanical model. In this regard, various mathematical extensions of the Gurson

porous material relation have been proposed over the past four decades to incorporate new fundamental material physics, including more complex material and hardening models (Tvergaard, 1981; Tvergaard, 1982; Mear & Hutchinson, 1985; Leblond et al., 1995; Lacroxi et al., 2016; Morin et al., 2017), initial and evolving void shape effects (Gologanu et al., 1993, 1994; Pardoen & Hutchinson, 2000; Ragab, 2004a, 2004b; Flandi & Leblond, 2005; Monchiet & Bonnet, 2013; Ueda et al., 2014), pressure-sensitivity and plastic dilatancy effects (Chew et al., 2006; Chew et al., 2007a, 2007b), matrix anisotropy effects (Castañeda & Zaidman, 1996; Benzerga & Besson, 2001; Lebensohn et al., 2004; Monchiet et al., 2004; Keralavarma & Benzerga, 2010; Morin et al., 2015), etc., which have extended the applicability of the Gurson model to different material systems as well as new loading conditions. However, many of these extensions necessitated significant experimental and computational efforts and took years to complete. Whether these extensions can be further generalized and applied to other target materials is also questionable.

Data-driven approaches using machine learning offer a promising path forward. Artificial neural networks (ANNs) have become a cornerstone in learning intricate data patterns through iterative training processes (Rosenblatt, 1958; Zhang et al., 1998; Schmidhuber, 2015; Moayedi et al., 2020; Yang et al., 2021), and have facilitated the quantification of grain boundary energy and stresses (Huber et al., 2018; Homer et al., 2019; Cui & Chew, 2022), detection of grain boundary dislocations (Noh & Chew, 2024), the identification of stress hotspots for fatigue cracking (Rovinelli et al., 2018; Pierson et al., 2019), as well as the predictions of crack growth and crack patterns in brittle and ductile materials (Wang et al., 2017; Moore et al., 2018; Hunter et al., 2019; Hsu et al., 2020; Wang et al., 2021; Buehler, 2022; Worthington & Chew, 2023). In the area of constitutive model development, ANNs have been used to predict diverse range of material properties, including density, porosity, hardness, and compressive strength (Hassan et al., 2009;

Bhattacharyay et al., 2016; Artrith & Urban, 2016; Armaghani & Asteris, 2021), optimize parameters for ductile fracture damage models (Abendroth & Kuna, 2003; Abendroth & Kuna, 2006; Shikalgar et al., 2020; Chen et al., 2021; Paermentier et al., 2021; Shafaie et al., 2022), forecast yield surfaces for ductile materials from porosity and mean stress information or microstructure images (Shen et al., 2020; Heidenreich et al., 2023), and even predict full-field solutions of elasto plastic materials under various loading conditions (Wang et al., 2021; Koric and Abueidda, 2023; He et al., 2023; He et al., 2024).

In this work, we harness the multivariable and highly generalized learning ability of ANNs to predict the macroscopic stress-strain constitutive response and the microscopic voiding characteristics (porosity, void shape) of void-containing RVEs under various deformation states. We train the ANNs on ground truth data based on finite element models of 3D RVEs, each containing a discrete spherical void, and integrate these neural networks in the finite element method (FEM) for tangent stiffness matrix and void evolution predictions. We assess the interpolative and extrapolative capabilities of the ANN approach in response to untrained loading conditions and porosities, and the ability of transfer learning to rapidly adapt these ANNs to other porous materials without significant retraining.

2. Background and Finite Element Modeling

Although the micromechanism of void nucleation, growth and coalescence is commonly associated with the ductile fracture of metals, this physical process has been observed in many engineering materials containing voids. When sufficient load is applied, these voids grow in tandem to the overall deformation, and a zone of high stress concentration then emanates between these voids, which nucleates secondary micro-voids. Driven by stored elastic energy, these micro-voids in turn undergo rapid plastic expansion; high stresses between these rapidly expanding

micro-voids subsequently drives the nucleation and growth of an additional set of micro-voids, and the entire process is repeated. An important aspect of this ductile fracture process is the cavitation instability phenomenon, which is known as the rapid nucleation and growth of one or several voids in a solid under sufficiently high hydrostatic stress. This rupture phenomenon was experimentally observed in several different material systems, including bonded rubber cylinders (Gent and Lindley, 1959), lead wire bonded to a surrounding glass cylinder (Ashby et al., 1989), metal foils sandwiched between ceramic plates (Dalgleish et al., 1988, 1989; Reimanis et al., 1990), and was numerically studied by a number of authors (Varias et al., 1991; Huang et al., 1991; Tvergaard et al., 1992; Huang et al., 1996; Faleskog and Shih, 1997; Tvergaard, 1998; Perrin & Leblond, 2000). Several analytical models have been developed to describe the cavitation-induced growth of voids in ductile materials. The early works of McClintock (1968) and Rice & Tracey (1969) derived mathematical relations for cylindrical and spherical void growth in infinite rigid plastic solids. They suggested that the growth of voids depends on the imposed equivalent plastic strain and the triaxiality ratio. Based on these concepts, Hancock & Mackenzie (1976) proposed a stress modified critical strain criterion, which provides a local index for the initiation of ductile fracture in metals as a function of plastic strain and stress triaxility, as well as a length-scale parameter.

2.1 Gurson constitutive model

The most widely known porous material model able to describe the plastic behavior of voided materials under multi-axial loading was put forth by Gurson (1977), and has a yield function (Gurson, 1977; Tvergaard, 1981)

$$\Phi(\Sigma_e, \Sigma_m, f) = \frac{\Sigma_e^2}{\sigma_0^2} + 2q_1 f \cosh\left(\frac{3q_2\Sigma_m}{2\sigma_0}\right) - 1 - q_3 f^2 = 0 \quad (1)$$

where σ_0 is the flow stress of the matrix, and Σ_e and Σ_m are the macroscopic equivalent stress and mean stress, respectively. The porosity or void volume fraction, f, is the damage variable, where $f = 0$ implies a fully-dense matrix material where (1) collapses to the von Mises yield criterion, i.e., $\sigma_e = \sigma_0$, where σ_e is the equivalent stress of the matrix, while $f = 1$ represents a completely voided material with no stress carrying capacity. The void growth rate obeys the volumetric plastic strain rate relation

$$\dot{f} = (1 - f)\mathrm{tr}\mathbf{d}^{\mathrm{p}} \tag{2}$$

where $\mathrm{tr}\mathbf{d}^{\mathrm{p}}$ is the trace of the plastic deformation rate $\mathbf{d}^{\mathrm{p}}$. In its early inception (represented by $q_1 = q_2 = q_3 = 1$ in (1)), the Gurson model considers a spherically symmetric void growth in a rigid, perfectly-plastic matrix under axisymmetric remote loading (Gurson, 1977). As such, the model could not account for elasto-plastic behavior (e.g., isotropic hardening), and could not physically describe void interaction effects, such as the flow localization between larger voids that drive cavity growth, void coalescence, and rupture. This led to the introduction of new adjustment "material" parameters (q_1, q_2, q_3) to the modified yield criterion to be calibrated against experiments or detailed numerical simulations (Tvergaard, 1981), such as by fitting an empirically measured deformation or stress-strain curve (Kozák & Vlček, 2005; Springmann & Kuna, 2005; Broggiato et al., 2007). Suitable (q_1, q_2, q_3) parameters for porous metal plasticity have been widely reported in the literature to account for isotropic hardening, as well as to improve predictions for periodically distributed voids at small void volume fractions (Gholipour et al., 2019; Erdoğan, 2021).

2.2 Representative volume element

The starting point for the development and validation of Gurson-type damage models has traditionally been finite element RVE studies. In this spirit, we perform finite element modeling

of 3D cubic unit cells using 8-noded C3D8 brick elements, each unit cell of dimensions $D \times D \times D$ with an initially spherical discrete void of radius R_0 at its center (Fig. 1a,b). The initial void volume fraction is defined by $f_0 = \frac{4}{3}\pi R_0^3/D^3$. We impose the displacement $u_3 = 0$ on the cell faces normal to the x_3-axis to maintain plane strain conditions. Pinning the corner nodes of the plane strain unit cell along $x_1 = x_2 = 0$, we subject all nodes on the positive x_1 and x_2 faces of the unit cell to elongations of l_1 and l_2 in the x_1 and x_2 directions, respectively. In the case of combined biaxial loading with shear deformation, we superimpose linearly varying displacements of u_2 $(u_1) = 0$ to l_{12} from x_1 $(x_2) = 0$ to D for all nodes along the cell faces normal to the x_2 (x_1)-axis to distort the unit cell to cause equal angular changes of $\theta = l_{12}/D$ under pure shear conditions (Fig. 1a). A multi-point constraint (MPC) subroutine is used to constrain all planar surfaces to remain planar after deformation. By setting $l_2 = \alpha_1 l_1$, and $l_{12} = \alpha_2 l_1$, where (α_1, α_2) denote the proportionality constants for each loading case, we achieve strain-controlled loading specified by the macroscopic logarithmic strain accounting for nonlinear geometry effects, $\boldsymbol{E} = \frac{1}{2}\ln\left(\boldsymbol{F}\cdot\boldsymbol{F}^{\boldsymbol{T}}\right)$, where $\boldsymbol{F}$ is the deformation gradient given by

$$\boldsymbol{F} = \begin{bmatrix} 1 + l_1/D & l_{12}/D & 0 \\ l_{12}/D & 1 + l_2/D & 0 \\ 0 & 0 & 1 \end{bmatrix} \tag{3}$$

The applied boundary/loading above enforces a parallel face constraint. While the RVE is periodic by nature, which allows for the enforcement of periodic boundary conditions (Kanit et al., 2006), we favor the kinematics uniform conditions since we seek to compare the macroscopic response of the RVE against a (single) Gurson-like porous computational cell element with the same equivalent boundary/loading conditions. The overall macroscopic stress tensor of each unit cell is computed from

$$\Sigma_{ij} = \frac{1}{V}\int_V \sigma_{ij}\, \mathrm{d}v \tag{4}$$

where σ_{ij} represents the local Cauchy stress within a voided cell, and V is the cell volume in the current deformed configuration. The macroscopic mean stress is given by $\Sigma_m = \Sigma_{kk}/3$, with the effective stress defined as $\Sigma_e = \sqrt{\frac{3}{2} S_{ij} S_{ij}}$, where S_{ij} is the deviatoric part of Σ_{ij}. The current void volume fraction in each unit cell is calculated from $f = V_f/V$, where V_f represents the current void volume obtained by numerical integration. In addition, the void shape evolution can be characterized by the major half-axis a and orthogonal (~minor) half-axis b in the in-plane direction, along with the orthogonal half-axis c in the out-of-plane direction (Fig. 1a,b). The matrix material is considered to be isotropic elasto-plastic, with a Young's modulus of $E = 68$ GPa, a Poisson's ratio of $\nu = 0.32$, and an initial yield stress of $\sigma_0 = 350$ MPa, representative of high-strength aluminum alloys; the plastic response is characterized by a J_2 flow theory, with the corresponding equivalent stress-strain response as shown in Fig. 1c under Mat 1. We use these same matrix material properties for Mat 1 in our Gurson model in (1), along with the adjustment parameters of $q_1 = 1.5, q_2 = 1, q_3 = (q_1)^2$ calibrated for high-strength aluminum alloys (Teng et al., 2014). Our finite element simulations are performed using the commercial finite element solver ABAQUS (Smith, 2009). We have performed mesh convergence studies, and show that the 24,000 elements used in modeling each 3D FEM RVE is sufficient to ensure accurate macroscopic stress-strain and porosity evolution predictions (see Fig. S1 of the Supplementary Materials).

We compare the macroscopic stress-strain and void evolution predictions of the Gurson model against 3D RVE data from FEM (henceforth termed as FEM data for brevity) for four initial porosities of $f_0 = 0.005$, 0.05, 0.10, and 0.15, covering the range of porosities applicable to both cavitated inclusions/particles in conventional metals and processing voids in additively-manufactured metals. In particular, a porosity of $f_0 = 0.15$ constitutes the upper porosity range of interest, since many studies (e.g. Xia & Shih, 1995) have alluded void coalescence to initiate at

$f = 0.15$, with an upper limit of $f = 0.2$ for the RVE to completely lose its stress carrying capacity. Under a plane strain uniaxial stress state in Fig. 2, the Gurson model accurately captures the evolution of (Σ_e, Σ_m, f) versus E_e for the lowest initial porosity of $f_0 = 0.005$, which is representative of the background microvoid fraction for conventional metals and alloys (Xia & Shih, 1995; Muro-Barrios et al., 2022) – an observation which is unsurprising, since the development of the Gurson model and the calibration of the adjustment (q_1, q_2, q_3) parameters were primarily for metallic alloys. However, the fundamental assumption of spherical void growth in a homogeneous deformation field in the Gurson model is not valid at high f_0, which leads to increasing deviation in the predicted (Σ_e, Σ_m, f) with f_0 under uniaxial tension. We remark that such high initial porosities are reflective of craze-voids ($f_0 = \sim 0.05$) in polymeric materials (Chew et al., 2007a, 2007b), and processing voids ($f_0 > 0.15$) in additively-manufactured metals (Cui et al., 2020; Muro-Barrios et al., 2022). Under combined biaxial tension and shear loading with $\alpha_1 = 3, \alpha_2 = 5$ in Fig. 3, significant deviation in the stress predictions of the Gurson model compared to FEM results are now observed across all f_0. Even at low initial porosities of $f_0 = 0.005$, the Gurson model severely underestimates the peak Σ_m, representing the caviation stress for rapid void growth. This small subset of results in Figs. 2 and 3 suggests a clear deficiency in the Gurson model when simulating unconventionally high initial porosities (e.g. processing voids in additively-manufactured metals), and/or when subjected to a complex deformation state.

3. Artificial Neural Network

To overcome the limitations of Gurson-type porous plasticity models, we adopt a series of ANNs illustrated in the flowchart in Fig. 4a to predict the constitutive material behavior (ANN-1), porosity evolution (ANN-2), and the detailed void shape evolution characteristics (ANN-3 to -5) of void-containing RVEs at incremental strains under plane strain conditions. All five ANN-x

share a common 12×1 input vector, which at load increment n, comprises of the current macroscopic strain tensor $\boldsymbol{E}^n$ (3 components: $E_{11}^n, E_{12}^n, E_{22}^n$), current macroscopic stress tensor $\boldsymbol{\Sigma}^{\mathrm{n}}$ (4 components: $\Sigma_{11}^n, \Sigma_{12}^n, \Sigma_{22}^n, \Sigma_{33}^n$), macroscopic strain increment tensor $\Delta\boldsymbol{E}^n$ (3 components: $\Delta E_{11}^n, \Delta E_{12}^n, \Delta E_{22}^n$), current porosity f^n (1 component), and the initial porosity of the voided cell f_0 (1 component). All inputs to the ANNs are normalized to [-1,1] by computing the mean and standard deviation of each input component.

3.1 Neural network interconnection

In a typical finite element code, the current stress increment tensor $\Delta\boldsymbol{\Sigma}^n$ at step n is related to the current strain increment tensor $\Delta\boldsymbol{E}^n$ through the tangent stiffness matrix $\mathbf{C}$,

$$\Delta\boldsymbol{\Sigma}^n = \mathbf{C}\colon \Delta\boldsymbol{E}^n \tag{5}$$

Because of the imposed plane strain boundary conditions of our RVEs ($u_3 = 0$ for all nodes on $x_3 = 0, D$), the components $\Delta E_{33}^n, \Delta E_{13}^n, \Delta E_{23}^n$ are always zero, and we can represent (5) in indicial form as

$$\begin{bmatrix} \Delta\Sigma_{11}^n \\ \Delta\Sigma_{22}^n \\ \Delta\Sigma_{33}^n \\ \Delta\Sigma_{12}^n \end{bmatrix} = \begin{bmatrix} \mathrm{C}_1 & \mathrm{C}_2 & \mathrm{C}_7 & \mathrm{C}_3 \\ \mathrm{C}_2 & \mathrm{C}_4 & \mathrm{C}_8 & \mathrm{C}_5 \\ \mathrm{C}_7 & \mathrm{C}_8 & 0 & \mathrm{C}_9 \\ \mathrm{C}_3 & \mathrm{C}_5 & \mathrm{C}_9 & \mathrm{C}_6 \end{bmatrix} \begin{bmatrix} \Delta E_{11}^{\mathrm{n}} \\ \Delta E_{22}^{\mathrm{n}} \\ 0 \\ \Delta E_{12}^{\mathrm{n}} \end{bmatrix} \tag{6}$$

where the symmetric 4×4 $\mathbf{C}$ matrix has 9 unique components. The components C_1 to C_6 are for computations of the stress increments $\Delta\Sigma_{11}^n, \Delta\Sigma_{12}^n, \Delta\Sigma_{22}^n$, while $\Delta\Sigma_{33}^n$ is computed from the off-diagonal C_7 to C_9 components. The direct output of ANN-1 is thus a 9×1 vector of the plane strain tangent stiffness matrix components C_1 to C_9, which are normalized with respect to the elastic modulus, from which we output the incremental stress tensor $\Delta\boldsymbol{\Sigma}^n$ and update the macroscopic stress tensor for the next strain increment,

$$\Sigma_{ij}^{n+1} = \Sigma_{ij}^n + \Delta\Sigma_{ij}^n \tag{7}$$

The implementation of a user material (UMAT) subroutine in Abaqus requires knowledge of both the incremental stress tensor in (7) and the tangential stiffness matrix components in (6), where the latter is used in a Newton-Rapson method to ensure that the converged solution satisfies equilibrium conditions. In our training of ANN-1, however, there is no convenient and computationally efficient way of extracting the stiffness matrix components of the entire RVE from our ground truth FEM data – a study on this subject is currently in progress. The macroscopic stress increment data in (7), however, can be computed at each incremental step from (4). Thus, in our training of ANN-1, we optimize the neural network to obtain the "stiffness matrix components" by minimizing the error in the macroscopic stress increment data in (7). In turn, we apply these "stiffness matrix components" in (5) to obtain an accurate computation of the macroscopic stress increment. While this does not guarantee uniqueness of the stiffness matrix components for a known strain increment, one can potentially accelerate the convergence in the Newton-Rapson iterative scheme with a line search algorithm. As an aside, the stiffness matrix components in (6) related to the true strain increment $\Delta E_{12}^{\mathrm{n}}$ have to be converted to the equivalent components for the engineering strain increment used by Abaqus UMAT; this simple conversion renders the stiffness matrix to be unsymmetric, but can be symmetrized to improve computational efficiency.

ANN-1 does not operate in isolation, and requires ANN-2 to provide an updated f^{n+1} as its output along with (7) to update the common input vector for the next $n = n + 1$ iteration. This iterative process allows for sequential updating of the stress and porosity values across the strain increments. During each strain increment n, we also output the void shape quantities $(\frac{a}{R_0}, \frac{b}{R_0}, \frac{c}{R_0})$ from ANN-3 to -5, respectively (Fig. 4a), representing the normalized major-, minor-, and out-of-plane half-axes of the deformed void (Fig. 1a,b).

In between the common input and the respective output layers of ANN-x are multiple hidden layers, as depicted in Fig. 4b. The nodes within each hidden layer apply transformations to the previous layer before passing them on to the next layer, while activation functions are imposed between the input/hidden and successive hidden/hidden layers. In this fashion, each ANN applies a series of weighting functions and biases to the input data to transform them into the output prediction. We compute the loss from the mean squared error (MSE) between the predicted output variables versus ground-truth data from FEM, except for ANN-1 where we base our MSE loss on the average of all the predicted $\Delta\Sigma_{ij}^{n}$ components. During backward propagation, the weights and biases are calibrated to minimize the MSE loss using the Adam's optimizer. With the updated weights and biases, each network will predict the new stiffness matrix components (ANN-1), new current porosity (ANN-2), and new deformed void shapes (ANN-3 to -5), correct the weights and biases by passing the error backwards (backward propagation), and iterate until convergence is achieved.

Thus, the neural networks (ANN-1 to -5) are interconnected, since the 4 components of current macroscopic stress (from ANN-1) and current porosity (from ANN-2) in the input are updated at each increment, and this common input is shared among all 5 ANNs. Having a single ANN predict the disparate outputs (macroscopic stress components, porosity, and major, minor, out-of-plane void axis) would require separate weightings for each of these output variables, which compromises accuracy and makes hyperparameter study (detailed in the subsection below) a challenge. Our decision to go with separate, but interconnected ANNs is in part motivated by the Gurson porous material model which comprises of both a yield function (1) and porosity evolution law (2), akin to ANN-1 and ANN-2, respectively. We view ANN-3 to -5 as additional modules

which do not contribute to ANN-1 and ANN-2, but use the information from ANN-1 and ANN-2 to make the evolving void shape predictions.

We remark that ANN-1 only captures the macroscopic plastic J_2-flow response of the RVE. Because we subject the RVE to monotonic loading in the majority of our studies, and there is effectively no elastic unloading. However, the history-dependency in the iterative update of the material state can be accounted for with an augmented stress update algorithm on von Mises plasticity, detailed in the Supplemental Materials (see Figs. S2-S4 and related discussions).

3.2 Hyperparameter studies

We train our ANNs on the stress-strain, porosity and void shape data generated by finite element simulations of our RVE model described in Section 2. We model 9 separate RVEs in FEM with different f_0 (0, 0.005, 0.01, 0.03, 0.05, 0.08, 0.1, 0.12, 0.15), and subject each RVE model to a series of loadings (a-d) below, which we in turn subdivide into individual load sets (1-4):

a. uniaxial stress –

set 1: tension/compression along x_1

set 3: tension/compression along x_2

b. pure shear –

set 1: $\theta > 0$

set 2: $\theta < 0$

c. biaxial loading –

set 1: $l_1 < 0\ \alpha_1 \in \{0\}, l_1 > 0\ \alpha_1 \in \{-6, -1, 0, 1, 5\}$

set 2: $l_1 < 0\ \alpha_1 \in \{-1, -1/6, 1, 5\}$

set 3: $l_1 > 0\ \alpha_1 \in \left\{-3, -\frac{1}{3}, \frac{1}{2}, 3, \infty\right\}, l_1 < 0\ \alpha_1 \in \left\{-3, -\frac{1}{3}, \frac{1}{2}, 3, \infty\right\}$

set 4: $l_1 > 0\ \alpha_1 \in \left\{-5, -2, -\frac{1}{2}, -\frac{1}{5}, -\frac{1}{6}, \frac{1}{6}, \frac{1}{5}, \frac{1}{4}, \frac{1}{3}, 2, 4, 6\right\},$

$$l_1 < 0\ \alpha_1 \in \left\{-6, -5, -2, -\frac{1}{2}, -\frac{1}{5}, \frac{1}{6}, \frac{1}{5}, \frac{1}{4}, \frac{1}{3}, 2, 4, 6\right\}$$

d. combined biaxial-shear loading –

set 1: $l_1 > 0\ (\alpha_1, \alpha_2) \in \{(1, -3), (1, 3)\}$

set 2: $l_1 < 0\ (\alpha_1, \alpha_2) \in \{(1, -3), (1, 3)\}$

set 3: $l_1 > 0\ (\alpha_1, \alpha_2) \in \left\{\left(\frac{5}{3}, -\frac{5}{3}\right), \left(\frac{5}{3}, \frac{5}{3}\right)\right\}$, $l_1 < 0\ (\alpha_1, \alpha_2) \in \left\{\left(\frac{5}{3}, -\frac{5}{3}\right), \left(\frac{5}{3}, \frac{5}{3}\right)\right\}$

set 4:

$$l_1 > 0, (\alpha_1, \alpha_2) \in \begin{Bmatrix} \left(\frac{3}{5}, -1\right), \left(\frac{1}{5}, -1\right), \left(\frac{1}{3}, -\frac{5}{3}\right), \left(\frac{1}{3}, -1\right), (5, -5), (3, -5), (3, -3), \\ (1, -5), (1, 5), (3, 3), (3, 5), (5, 5), \left(\frac{1}{3}, 1\right), \left(\frac{1}{3}, \frac{5}{3}\right), \left(\frac{1}{5}, 1\right), \left(\frac{3}{5}, 1\right) \end{Bmatrix},$$

$$l_1 < 0, (\alpha_1, \alpha_2) \in \begin{Bmatrix} \left(\frac{3}{5}, -1\right), \left(\frac{1}{5}, -1\right), \left(\frac{1}{3}, -\frac{5}{3}\right), \left(\frac{1}{3}, -1\right), (5, -5), (3, -5), (3, -3), \\ (1, -5), (1, 5), (3, 3), (3, 5), (5, 5), \left(\frac{1}{3}, 1\right), \left(\frac{1}{3}, \frac{5}{3}\right), \left(\frac{1}{5}, 1\right), \left(\frac{3}{5}, 1\right) \end{Bmatrix}$$

Cumulatively, these combined load sets (1+2+3+4) constitute 90 unique loading cases for each f_0.

In our FEM models, we incrementally increase the applied strain for each load case, and determine from finite element the macroscopic stress increment, current porosity, along with the current major-, minor-, and out-of-plane half-axes of the deformed void shape. Thus, the FEM data at each strain increment provides a single input-output ground truth data point for training of all five ANNs. Because the loading path for each load case consists of approximately 100 increments, the 90 loading paths across 9 simulated RVEs with varying f_0 results in a total of 81,296 data points, which we split into training (65,038), validation (8,129), testing (8,129) datasets in an 8:1:1 ratio. We find that varying the size of the loading (strain) increments has little bearing on the predictive performance of our ANNs once the increments are sufficiently small, as illustrated in Fig. S5 of the Supplementary Materials.

We conduct hyperparameter testing to identify the optimal architecture (number of hidden layers, number of nodes per layer), learning rate, batch size, and choice of activation function for each ANN-x. We start with five separate instantiations of each ANN-x with randomly assigned initial weights and biases, and train all five instantiations for each specified hyperparameter setting for 200 epochs using the training dataset. For each ANN-x instantiation, we monitor the MSE loss from the training dataset, as well as the validation dataset to detect potential overfitting. We select the ANN-x configuration at the epoch where each instantiation has the smallest validation loss, and compute the testing loss from all these instantiations. We record the mean validation loss and mean testing loss from these five ANN-x instantiations. In most cases, we select the instantiation with the lowest validation loss as the optimal network structure for the specified hyperparameter setting; our testing losses further confirm the suitability of the optimized hyperparameter setting.

We summarize the results of our hyperparameter study in Tables S1 to S5 of the Supplementary Materials. We find that ANN-1 (stress-strain predictions) requires a relatively deep neural network architecture of 4 hidden layers with 350 nodes per hidden layer, compared to ANN-2 (porosity predictions) which requires a smaller network structure of 2 hidden layers with 70 nodes per hidden layer. Depending on the void shape feature (major, minor, out-of-plane half-axis) for ANN-3 to -5, the optimal number of layers ranges from 3 to 6 with 120 to 170 nodes per hidden layer. Our studies show that all of our network structures are highly sensitive to the learning rate, which is optimal at 0.001 for ANN-4 and 0.0005 for the remaining ANN-x. The optimal batch size varies from 64 to 128 across our ANN-x. The ReLU and LeakyReLU activation functions consistently provide (close to) the lowest MSE loss across all ANN-x, compared to the Exponential Linear Unit (ELU), Scaled Exponential Linear Units (SELU), Sigmoid, LogSigmoid, and Hyperbolic Tangent (tanh) activation functions. Given the similar performance of ReLU and

LeakyReLU, we select the former for all our ANN-x configurations. In subsequent studies, we subject a 4-noded bilinear plane strain element to finite deformation, utilizing the optimized ANN-x architectures in a user material (UMAT) subroutine implemented in ABAQUS to compute the tangent stiffness matrix, stress increment, porosity, and void shape features at incremental strains. Because the loading increments and even some of the applied load cases of these ANN-based UMAT simulations are outside of the original ANN training/validation/testing datasets, our subsequent comparison between the ground truth FEM-RVE data versus the ANN-based UMAT computations provide the true independent testing crucial for reliable model evaluation.

We train our above ANNs on the complete load set (1+2+3+4). We confirm the adequacy of this load set, by comparing the evolution of the macroscopic stress components (Fig. 5) and porosity (Fig. 6) with equivalent strain, as predicted by our ANNs (solid line) versus ground truth data from FEM (symbols) for the extreme initial porosities of $f_0 = 0.005$ (blue) and 0.15 (red) under combined biaxial tension and shear loading characterized by $\alpha_1 = 3, \alpha_2 = 5$ – a load case which proves to be challenging for the Gurson constitutive model (Fig. 3). Our ANN predictions are in near-perfect agreement with FEM results for both f_0 when the ANNs are trained on the complete load set (1+2+3+4). In contrast to the Gurson model (Fig. 3), our ANNs for low $f_0 = 0.005$ accurately captures the non-monotonic Σ_{12} shear stress evolution, along with the hardening and softening profile of the normal ($\Sigma_{11}, \Sigma_{22}, \Sigma_{33}$) stress components. At high f_0 of 0.15, our ANNs also quantitatively capture the saturation of these normal stress components, along with the monotonically increasing Σ_{12} with E_e; ANN-2 also perfectly predicts the distinctly different porosity evolutions for both f_0, compared to the Gurson model where deviations in the post-cavitation void growth response of $f_0 = 0.005$ are observed (Fig. 3). We have separately trained ANN-1 and ANN-2 on reduced load set combinations of (1), (1+2), and (1+2+3). As shown in

Figs. 5 and 6, we observe notable performance decrease of these ANNs versus the original ANNs trained on the full dataset, especially for low $f_0 = 0.005$ (blue) where an order-of-magnitude increase in porosity, triggered by cavitation, results in significant material softening and loss of stress-carrying-capacity. Nevertheless, our ANN predictions even when trained on the smallest load set (1) or (1+2) are in far better agreement with FEM results compared to the Gurson model (Fig. 3). Unless otherwise stated, our ANNs herein are trained on the full load set (1+2+3+4).

4. Results and Discussions

4.1 Interpolation versus extrapolation

Our results in Figs. 5 and 6 demonstrate that the ANNs are capable of reproducing the incremental stress-strain and porosity evolution response they have been trained on (biaxial tension + shear with $\alpha_1 = 3, \alpha_2 = 5$). This is further evidenced by the near perfect agreement between our ANN predictions versus FEM results for $f_0 = 0.05$ under a pure biaxial loading state ($\alpha_2 = 0$) with $\alpha_1 = 1$ representing equi-biaxial straining (square symbol – ANN, solid black line – FEM), and $\alpha_1 = 6$ (triangular symbol – ANN, dashed black line – FEM) in Fig. 7. We remark that even when "tested" on the exact load case the ANNs have been trained for, these ANNs are still interpolating between the learned strain or strain increment data, since both the current strain ($\boldsymbol{E}^n$) and the current strain increment ($\Delta\boldsymbol{E}^n$) at step n will conceivably be different from the values in the training dataset. Here, we evaluate the biaxial loading response of these ANNs, trained on fixed α_1 displacement ratios, to untrained biaxial loading scenarios where α_1 varies with E_e.

Under a monotonically increasing α_1 from 1 to 6 (blue in Fig. 7), the post-peak ANN predictions for Σ_e deviate slightly from FEM, but both the evolution of Σ_m and f are perfectly captured by our ANN. In the case where α_1 monotonically decreases from 6 to 1 (red in Fig. 7), the peak to initial post-peak regime for Σ_e is again correctly captured by our ANN, but the final

softening regime after significant loss of stress-carrying capacity deviates from FEM results. Nevertheless, the evolution of both Σ_m and f, which are arguably the more important quantities under a biaxial strain state, are well captured by our ANN. In fact, even the interesting trend of f initially tracing the porosity curve for $\alpha_1 = 6$, and later deviating to merge with the porosity curve for $\alpha_1 = 1$ at higher E_e, is correctly predicted by our ANN.

We observe similar trends under biaxial tension loading with α_1 increasing from 1 to 6 and back to 1 (blue in Fig. 8). Deviations between ANN and FEM results are observed in the post-peak Σ_e, but the mean stress and porosity evolution – especially the sudden change in the porosity gradient corresponding to the sharp transition in α_1 – are very well captured by our ANN. Similar trends are also observed when α_1 decreases from 6 to 1 and back to 6 (red in Fig. 8). While the post-peak ANN predictions of Σ_e can conceivably be improved with more representative training load sets, we remark that the RVE response under a biaxial strain state will primarily be driven by the hydrostatic rather than deviatoric stress component. Since Σ_m is consistently well predicted by our ANNs, our resulting void growth (and hence damage evolution) predictions are also very accurate.

The initial porosity is an input parameter to the Gurson yield function in (1). Similar, f_0 is a common input parameter in our ANN-x (Fig. 4), and we have trained these ANNs across an extensive range of f_0 from 0.005 to 0.15. We find that including $f_0 = 0$ in our training dataset, per our hyperparameter studies in Section 3.2, biases our (Σ_e, Σ_m) predictions to be slightly higher than the actual FEM results (Fig. S6 in the Supplementary Materials), since this undamaged material does not exhibit the material softening characteristics common to the rest of the training dataset for $f_0 \neq 0$. Accordingly, we have retrained our ANNs by removed the dataset associated with $f_0 = 0$ in our subsequent studies. We demonstrate the remarkable ability of our augmented

ANNs to accurately predict the evolution of (Σ_e, Σ_m, f) with E_e under a combination of biaxial tension with shear ($\alpha_1 = 3, \alpha_2 = 5$) across a wide range of initial porosities in Fig. 9. In fact, all ANN predictions (symbols) are in near-perfect agreement with FEM data (lines), be it for initial porosities within the training dataset (black), for untrained "interpolated" initial porosity of $f_0 = 0.02$, or for an order-of-magnitude larger untrained "extrapolated" initial porosity of $f_0 = 0.2$. Note that $f_0 = 0.2$ is the upper porosity limit of interest, since it represents the critical porosity for void coalescence and crack advance in fracture problems (Pardoen and Hutchinson, 2000). Although some levels of extrapolation to unseen data (e.g. Figs. 7-9) are possible with our neural network models, caution should be exercised when performing such extrapolation far beyond the load cases in the training datasets of the networks. For example, our ANNs, primarily trained on strain-controlled load cases, cannot accurately extrapolate the predictions to the macroscopic response of stress-controlled load cases without including these load cases within the training dataset.

While the current porosity f is widely regarded as the sole material damage parameter, studies show that the onset of void coalescence also depends on the shape of the void (Pardoen and Hutchinson, 2000). In ductile fracture problems, the voids within the process zone remain nearly spherical during initial loading. Once the critical (mean) cavitation stress is reached, unstable voiding occurs leading to an increasingly oblate void, which significantly reduces the intervoid separation distance and accelerates the coalescence of voids (Chew et al., 2007b). Thus, the criterion for void coalescence could conceivably depend on the shape of the void, in addition to its porosity (Tvergaard and Hutchinson, 2002). In this regard, a limitation of the Gurson model is its presumption of spherically symmetric void growth. Because we train our ANNs on RVE models containing discrete voids in FEM, our *macroscopic* ANN predictions of porosity and stress

evolutions do not suffer from this inherent limitation of the Gurson model. Furthermore, by tagging on ANN-3, -4, and -5 to our neural network framework, we are also able to elucidate the evolving major ($\frac{a}{R_0}$), minor ($\frac{b}{R_0}$), and out-of-plane ($\frac{c}{R_0}$) half-axes representing the *microscopic* void shape during deformation. In concert with the macroscopic stress/porosity predictions, such microscopic void shape predictions can provide rich fundamental insights into the detailed micromechanics of fracture and failure, while bypassing detailed finite element modeling. We show in Fig. 10 the ANN versus FEM predictions of the evolving void shapes under a combination of biaxial tension with shear ($\alpha_1 = 3, \alpha_2 = 5$) across a wide range of initial porosities. Similar to our predictions of (Σ_e, Σ_m, f) with E_e in Fig. 9, our void shape predictions of ($\frac{a}{R_0}, \frac{b}{R_0}, \frac{c}{R_0}$) in Fig. 10 are in near perfect agreement with FEM data, across both trained (0.005, 0.01, 0.03, 0.05, 0.08, 0.1, 0.12, 0.15) and untrained (0.02 – interpolative, 0.2 – extrapolative) initial porosity datasets. By assuming an ellipsoidal void shape with the three semi-axes of the ellipsoid represented by the microstructural void shape information (a, b, c) from ANN-3 to -5, one can compute the ellipsoid void volume ($\frac{4}{3}\pi abc$), and in turn, the porosity f of the RVE. As shown in Fig. S7 of the Supplementary Materials, this indirect approach of obtaining the porosity evolution from the void shape characteristics (ANN-3 to -5) is found to be in near perfect agreement with direct porosity predictions (ANN-2), which exemplifies the intimate connection between the microscopic void feature predictions and the macroscopic damage predictions in our neural network modeling.

4.2 Transfer learning

The calibration parameters (q_1, q_2, q_3) in (1) were introduced in-part to adapt the Gurson yield function to different σ_0/E and hardening parameters, by matching the predicted stress-strain response to that of an RVE model in FEM under relatively simple load cases, such as uniaxial stress. A limitation of our ANNs is that they rely on matrix material properties used in the

generated training dataset (Mat 1 in Fig. 1c). Thus, to adapt the ANNs to a different matrix material (e.g. Mat 2 or Mat 3 in Fig. 1c), we would ideally have to re-train our ANNs on a new dataset based on the updated matrix material properties. Nevertheless, one of the key advantages of machine learning is the ability to perform transfer learning. Instead of training a model from scratch for each new task, transfer learning leverages the knowledge gained from solving a source task to improve learning and performance on a target task, which helps to reduce training time, improve generalization, and facilitate domain adaption (Iman et al., 2023). Rather than training ANN-1 to -5 from scratch for each new material model, we could instead initialize the weights and biases of this new set of ANNs based on the earlier trained neural networks for the original material, which could substantially reduce the size of the new training dataset.

We investigate the transfer learnability of ANN-1 and -2, trained on Mat 1 in Fig. 1c, towards two new matrix materials with radically different stress-strain responses: Mat 2 and Mat 3 in Fig. 1c. Mat 2 has the same elastic properties ($E = 68$ GPa$, \nu = 0.32$) as Mat 1, but features a much smaller initial yield stress ($\sigma_0 = 156$ MPa), and a distinct plastic behavior that plateaus before undergoing significant rehardening. Conversely, Mat 3 is considerably softer than Mat 1 ($E = 2$ GPa$, \nu = 0.4$), and exhibits strain-hardening followed by softening, before saturating at its initial yield stress of $\sigma_0 = 32.5$ MPa. While both matrix material models differ significantly from Mat 1, the underlying micromechanisms of void growth are still the same, leading one to presume that the parametric effects of initial porosity, loading states, etc., constituting the low-level features would be somewhat similar regardless of the type of matrix material.

We seek the use of transfer learning to preserve the low-level features in our pre-trained ANN-x (on Mat 1), while reducing (1) the datasets (for Mat 2/3) needed to fine-tune the networks and (2) the computational time or expense necessary for retraining. Since the initial few layers of

the neural networks are known the encompass the most general (low-level) features of the model, we freeze the bottom few layers of ANN-1 so that these layer weights and biases, initially trained on Mat 1, are unchanged when backpropagation is performed during training. Thus, fine-tuning of the weights and biases is only confined to the remaining unfrozen upper layers in ANN-1, which significantly speeds up the training of the network. Our ANN-1 has 4 hidden layers, which are labeled L_1 to L_4 in ascending order. The more frozen layers we have, the more we inherit features from our pre-trained ANN-1. By doing so, we are assuming that the new macroscopic stress evolution for Mat 2/3 contain many low-level features similar to the pre-trained ANN-1 for Mat 1. In contrast, freezing too many layers forces the ANN to apply both low- and high-level features in its pre-training towards Mat-2. Here, we study this delicate balance by systematically varying the number of frozen layers in ANN-1, while fine-tuning the weights and biases preceding the remaining free hidden and output layer(s) initialized on Mat 1, on the new training dataset for Mat 2/3. Given the shallow (2 hidden layer) network structure of ANN-2, we concurrently fine-tune the weights and biases of all hidden layers for ANN-2 from their initial values based on Mat 1.

We summarize our transfer learning results for Mat 2 with initial porosities of $f_0 = 0.005$ and 0.15 in Figs. 11 and 12 under combined biaxial tension with shear ($\alpha_1 = 3, \alpha_2 = 5$), and include the corresponding error metrics in Table S6 of the Supplementary Materials. We remark that this specific load case is outside of our significantly reduced training load set (1+2) for Mat 2 (versus load set 1+2+3+4 for Mat 1), used to fine-tune the weights and biases preceding the free hidden and output layer(s). Our results demonstrate that freeing the last 2 layers of ANN-1 (i.e., L_3 and L_4) is sufficient to allow the neural network to attain comparable accuracy to FEM results for Mat 2. In the absence of transfer learning, ANN-1 and -2 trained on this reduced load set (1+2) with *randomly* initialized weights and biases (dashed black lines) yield very poor (Σ_e, Σ_m, f)

predictions for $f_0 = 0.005$. Very similar transfer learning results are observed for ANN-1 and -2 fine-tuned on training load set (1+2) for Mat 3 in Figs. 13 and 14; we achieve excellent predictions by freezing L_1 and L_2 in ANN-1 and fine-tuning the remaining weights and biases. For both Mat 2 and Mat 3, we observe that the ANN predictions can be improved with more free hidden layers. For Mat 2 with $f_0 = 0.005$, for example, the porosity predictions do not vary significantly with the number of free hidden layers, but the (equivalent, mean) stress losses decrease from (5.33e-4, 2.20e-3) by freeing only L_4, to (3.82e-4, 4.23e-3) by freeing L_3 and L_4, and to (2.69e-4, 8.47e-4) by freeing L_2-L_4 in ANN-1. Similarly for Mat 3 with $f_0 = 0.15$, the (equivalent, mean) stress losses systematically decrease from (1.43e-6, 1.28e-6) by freeing only L_4, to (1.35e-6, 4.21e-6) by freeing L_3 and L_4, and to (9.21e-7, 7.20e-7) by freeing L_2-L_4 in ANN-1.

When there are no frozen layers, we fine-tune the weights and biases of the entire ANN-1 on the dataset for Mat 2/3. In the case of Mat 3, our results show that very high ANN accuracies can still be achieved by fine-tuning the weights and biases of the entire network on an even smaller load set 1 (blue symbols in Figs. 13 and 14). We remark that even when all layers are free, knowledge from the pre-trained ANN-1 on Mat 1 is still transferred in the form of the initial weights and biases. Our hyperparameter studies show that this initialization is important, since significant changes to the predictive accuracies can result from poor initialization choices. Using randomly assigned initial weights and biases, and training the same ANN-1 and -2 on load set 1 (blue lines), we observe significantly reduced accuracies for $f_0 = 0.15$, with completely erroneous predictions for $f_0 = 0.005$.

5. Concluding Remarks

Data-driven approaches are revolutionizing the constitutive modeling of materials. Using a series of neural networks, trained on the deformation response of void-containing unit cells in finite

element, we demonstrate the ability of this data-driven approach to accurately quantify the stress-strain constitutive behavior and the void (damage) evolution response of the unit cell under strain-controlled, monotonic loadings; in the case of elastic unloading/reloading, the history-dependency in the iterative update of the material state can also be accounted for with an augmented stress update algorithm on von Mises plasticity (see Figs. S2-S4 and related discussions in Supplemental Materials). The neural networks are capable of interpolative predictions as well as some levels of extrapolation to untrained loading conditions and initial porosities, and are able to provide quantitative measures of the evolving shapes of the deformed voids. Through transfer learning, our results show that the neural networks can be readily extended to different matrix materials with significantly reduced datasets and reduced training time.

In contrast to the Gurson constitutive model which assumes a rigid-plastic response along with spherical symmetric void growth and axisymmetric loading in its derivation (Gurson, 1977), our neural networks for porous material failure are only limited by the assumptions inherent in the (finite element) models used to generate the dataset for training of these networks. By encompassing low to very high initial porosities in the training dataset, our neural networks are applicable to simulating the deformation response of a wide range of porous material structures, from the inclusions and cavities ($f_0 \sim 0.005$) in conventional metal alloys (Stone et al., 1985; Faleskog & Shih, 1997), to processing voids ($f_0 \sim 0.15$) in additively-manufactured metals (Cui et al., 2020; Muro-Barrios et al., 2022). As long as the void evolution mechanisms are similar, the low-level features in these neural networks can also be "transferred" to other matrix materials (e.g., polymers, ceramics, cellular structures, fiber-reinforced composites), which extends the applicability of these neural networks to general porous material systems without the need for significant re-training.

Ultimately, the neural network approach allows for bridging of scales to achieve rapid constitutive modeling of materials. A successful neural network model relies on having input-output data spanning the desired loading conditions (stress- or strain-controlled loading, uniaxial or multiaxial loading) and microstructural complexities (initial void size, shape, distribution) to allow for data interpolation and to a lesser extent, data extrapolation. However, this training of the neural networks on data, and data alone, allows for homogenization of complex microstructural features (voids), yet with the ability for this reduced-order model to quantify the deformation characteristics of these features (porosity, void shapes), which are critical for elucidating the micromechanics of material damage and failure in fracture and fatigue problems.

Acknowledgements

The authors acknowledge the support provided by the National Science Foundation under Grant Nos: NSF-CMMI-2009684, NSF-DMR-2406764, and NSF-CMMI-2425707. The use of the Advanced Cyberinfrastructure Coordination Ecosystem: Services & Support (ACCESS), through allocations MAT240041, MAT230069, MAT210031, and MAT230055, and TACC Frontera through allocation MSS22006, is gratefully acknowledged.

References

Abendroth, M., Kuna, M., 2003. Determination of deformation and failure properties of ductile materials by means of the small punch test and neural networks. computational materials Science, 28(3-4), pp.633-644. https://doi.org/10.1016/j.commatsci.2003.08.031.

Abendroth, M., Kuna, M., 2006. Identification of ductile damage and fracture parameters from the small punch test using neural networks. Engineering fracture mechanics, 73(6), pp.710-725. https://doi.org/10.1016/j.engfracmech.2005.10.007.

Abuzaid, W., Oral, A., Sehitoglu, H., Lambros, J., Maier, H.J., 2013. Fatigue crack initiation in Hastelloy X–the role of boundaries. Fatigue & Fracture of Engineering Materials & Structures, 36(8), pp.809-826. https://doi.org/10.1111/ffe.12048.

Armaghani, D.J., Asteris, P.G., 2021. A comparative study of ANN and ANFIS models for the prediction of cement-based mortar materials compressive strength. Neural Computing and Applications, 33(9), pp.4501-4532. https://doi.org/10.1007/s00521-020-05244-4.

Artrith, N., Urban, A., 2016. An implementation of artificial neural-network potentials for atomistic materials simulations: Performance for TiO2. Computational Materials Science, 114, pp.135-150. https://doi.org/10.1016/j.commatsci.2015.11.047.

Ashby, M.F., Blunt, F.J., Bannister, M., 1989. Flow characteristics of highly constrained metal wires. Acta metallurgica, 37(7), pp.1847-1857. https://doi.org/10.1016/0001-6160(89)90069-2.

Barenblatt, G.I., 1962. The mathematical theory of equilibrium cracks in brittle fracture. Advances in applied mechanics, 7, pp.55-129. https://doi.org/10.1016/S0065-2156(08)70121-2.

Benzerga, A.A., Besson, J., 2001. Plastic potentials for anisotropic porous solids. European Journal of Mechanics-A/Solids, 20(3), pp.397-434. https://doi.org/10.1016/S0997-7538(01)01147-0.

Bhattacharyay, D., Kocaefe, D., Kocaefe, Y., Morais, B., Gagnon, M., 2016. Application of the artificial neural network (ANN) in predicting anode properties. Light Metals 2013, pp.1189-1194. https://doi.org/10.1007/978-3-319-65136-1_201.

Broggiato, G.B., Campana, F., Cortese, L., 2007. Identification of material damage model parameters: an inverse approach using digital image processing. Meccanica, 42, pp.9-17. https://doi.org/10.1007/s11012-006-9019-5.

Buehler, M.J., 2022. Modeling atomistic dynamic fracture mechanisms using a progressive transformer diffusion model. Journal of Applied Mechanics, 89(12), p.121009. https://doi.org/10.1115/1.4055730.

Castañeda, P.P., Zaidman, M., 1994. Constitutive models for porous materials with evolving microstructure. Journal of the Mechanics and Physics of Solids, 42(9), pp.1459-1497. https://doi.org/10.1016/0022-5096(94)90005-1.

Chan, K.S., 2010. Roles of microstructure in fatigue crack initiation. International Journal of Fatigue, 32(9), pp.1428-1447. https://doi.org/10.1016/j.ijfatigue.2009.10.005.

Chen, D., Li, Y., Yang, X., Jiang, W., Guan, L., 2021. Efficient parameters identification of a modified GTN model of ductile fracture using machine learning. Engineering Fracture Mechanics, 245, p.107535. https://doi.org/10.1016/j.engfracmech.2021.107535.

Chew, H.B., Guo, T.F., Cheng, L., 2005. Vapor pressure and residual stress effects on failure of an adhesive film. International Journal of Solids and Structures, 42(16-17), pp.4795-4810. https://doi.org/10.1016/j.ijsolstr.2005.01.012.

Chew, H.B., Guo, T.F., Cheng, L., 2006. Effects of pressure-sensitivity and plastic dilatancy on void growth and interaction. International Journal of Solids and Structures, 43(21), pp.6380-6397. https://doi.org/10.1016/j.ijsolstr.2005.10.014.

Chew, H.B., Guo, T.F., Cheng, L., 2007a. Pressure-sensitive ductile layers–I. Modeling the growth of extensive damage. International Journal of Solids and Structures, 44(7-8), pp.2553-2570. https://doi.org/10.1016/j.ijsolstr.2006.08.005.

Chew, H.B., Guo, T.F., Cheng, L., 2007b. Pressure-sensitive ductile layers–II. 3D models of extensive damage. International journal of solids and structures, 44(16), pp.5349-5368. https://doi.org/10.1016/j.ijsolstr.2007.01.002.

Chew, H.B., Hong, S., Kim, K.S., 2009. Cohesive zone laws for void growth—II. Numerical field projection of elasto-plastic fracture processes with vapor pressure. Journal of the Mechanics and Physics of Solids, 57(8), pp.1374-1390. https://doi.org/10.1016/j.jmps.2009.04.001.

Chew, H.B., 2013. Inverse extraction of interfacial tractions from elastic and elasto-plastic far-fields by nonlinear field projection. Journal of the Mechanics and Physics of Solids, 61(1), pp.131-144. https://doi.org/10.1016/j.jmps.2012.08.007.

Chew, H.B., 2014. Cohesive zone laws for fatigue crack growth: Numerical field projection of the micromechanical damage process in an elasto-plastic medium. International Journal of Solids and Structures, 51(6), pp.1410-1420. https://doi.org/10.1016/j.ijsolstr.2013.12.033.

Cui, Y., Gao, Y.F., Chew, H.B., 2020. Two-scale porosity effects on cohesive crack growth in a ductile media. International Journal of Solids and Structures, 200, pp.188-197. https://doi.org/10.1016/j.ijsolstr.2020.04.035.

Cui, Y., Chew, H.B., 2022. Machine-learning prediction of atomistic stress along grain boundaries. Acta Materialia, 222, p.117387. https://doi.org/10.1016/j.actamat.2021.117387.

Dalgleish, B.J., Lu, M.C., Evans, A.G., 1988. The strength of ceramics bonded with metals. Acta Metallurgica, 36(8), pp.2029-2035. https://doi.org/10.1016/0001-6160(88)90304-5.

Dalgleish, B.J., Trumble, K.P., Evans, A.G., 1989. The strength and fracture of alumina bonded with aluminum alloys. Acta Metallurgica, 37(7), pp.1923-1931. https://doi.org/10.1016/0001-6160(89)90077-1.

Dugdale, D.S., 1960. Yielding of steel sheets containing slits. Journal of the Mechanics and Physics of Solids, 8(2), pp.100-104. https://doi.org/10.1016/0022-5096(60)90013-2.

Erdoğan, C., 2021. Numerical implementation and analysis of a porous plasticity model for ductile damage prediction. Master's thesis, Middle East Technical University. https://hdl.handle.net/11511/89746.

Faleskog, J., Shih, C.F., 1997. Micromechanics of coalescence—I. Synergistic effects of elasticity, plastic yielding and multi-size-scale voids. Journal of the Mechanics and Physics of Solids, 45(1), pp.21-50. https://doi.org/10.1016/S0022-5096(96)00078-6.

Flandi, L., Leblond, J.B., 2005. A new model for porous nonlinear viscous solids incorporating void shape effects–I: Theory. European Journal of Mechanics-A/Solids, 24(4), pp.537-551. https://doi.org/10.1016/j.euromechsol.2005.03.003.

Foehring, D., Chew, H.B., Lambros, J., 2018. Characterizing the tensile behavior of additively manufactured Ti-6Al-4V using multiscale digital image correlation. Materials Science and Engineering: A, 724, pp.536-546. https://doi.org/10.1016/j.msea.2018.03.091.

Gent, A.N., Lindley, P.B., 1959. Internal rupture of bonded rubber cylinders in tension. Proceedings of the Royal Society of London. Series A. Mathematical and Physical Sciences, 249(1257), pp.195-205. https://doi.org/10.1098/rspa.1959.0016.

Gholipour, H., Biglari, F.R., Nikbin, K., 2019. Experimental and numerical investigation of ductile fracture using GTN damage model on in-situ tensile tests. International Journal of Mechanical Sciences, 164, p.105170. https://doi.org/10.1016/j.ijmecsci.2019.105170.

Gologanu, M., Leblond, J.B., Devaux, J., 1993. Approximate models for ductile metals containing non-spherical voids—case of axisymmetric prolate ellipsoidal cavities. Journal of the Mechanics and Physics of Solids, 41(11), pp.1723-1754. https://doi.org/10.1016/0022-5096(93)90029-F.

Gologanu, M., Leblond, J.B., Devaux, J., 1994. Approximate models for ductile metals containing nonspherical voids—case of axisymmetric oblate ellipsoidal cavities. https://doi.org/10.1115/1.2904290.

Guo, W., Wang, C.H., Rose, L.R.F., 1999. The influence of cross‐sectional thickness on fatigue crack growth. Fatigue & Fracture of Engineering Materials & Structures, 22(5), pp.437-444. https://doi.org/10.1046/j.1460-2695.1999.00176.x.

Gurson, A.L., 1977. Continuum theory of ductile rupture by void nucleation and growth: Part I—Yield criteria and flow rules for porous ductile media. https://doi.org/10.1115/1.3443401.

Hancock, J.W., Mackenzie, A.C., 1976. On the mechanisms of ductile failure in high-strength steels subjected to multi-axial stress-states. Journal of the Mechanics and Physics of Solids, 24(2-3), pp.147-160. https://doi.org/10.1016/0022-5096(76)90024-7.

Hassan, A.M., Alrashdan, A., Hayajneh, M.T., Mayyas, A.T., 2009. Prediction of density, porosity and hardness in aluminum–copper-based composite materials using artificial neural network. Journal of materials processing technology, 209(2), pp.894-899. https://doi.org/10.1016/j.jmatprotec.2008.02.066.

He, J., Koric, S., Kushwaha, S., Park, J., Abueidda, D., Jasiuk, I., 2023. Novel DeepONet architecture to predict stresses in elastoplastic structures with variable complex geometries and loads. Computer Methods in Applied Mechanics and Engineering, 415, p.116277. https://doi.org/10.1016/j.cma.2023.116277.

He, J., Kushwaha, S., Park, J., Koric, S., Abueidda, D., Jasiuk, I., 2024. Sequential Deep Operator Networks (S-DeepONet) for predicting full-field solutions under time-dependent loads. Engineering Applications of Artificial Intelligence, 127, p.107258. https://doi.org/10.1016/j.engappai.2023.107258.

Heidenreich, J.N., Gorji, M.B., Mohr, D., 2023. Modeling structure-property relationships with convolutional neural networks: Yield surface prediction based on microstructure images. International Journal of Plasticity, 163, p.103506. https://doi.org/10.1016/j.ijplas.2022.103506.

Homer, E.R., Hensley, D.M., Rosenbrock, C.W., Nguyen, A.H., Hart, G.L., 2019. Machine-learning informed representations for grain boundary structures. Frontiers in Materials, 6, p.168. https://doi.org/10.3389/fmats.2019.00168.

Hong, S., Chew, H.B., Kim, K.S., 2009. Cohesive-zone laws for void growth—I. Experimental field projection of crack-tip crazing in glassy polymers. Journal of the Mechanics and Physics of Solids, 57(8), pp.1357-1373. https://doi.org/10.1016/j.jmps.2009.04.003.

Hsu, Y.C., Yu, C.H., Buehler, M.J., 2020. Using deep learning to predict fracture patterns in crystalline solids. Matter, 3(1), pp.197-211. https://doi.org/10.1016/j.matt.2020.04.019.

Huang, Y., Hutchinson, J.W., Tvergaard, V., 1991. Cavitation instabilities in elastic-plastic solids. Journal of the Mechanics and Physics of Solids, 39(2), pp.223-241. https://doi.org/10.1016/0022-5096(91)90004-8.

Huang, Y., Hu, K.X., Yeh, C.P., Li, N.Y., Hwang, K.C., 1996. A model study of thermal stress-induced voiding in electronic packages. https://doi.org/10.1115/1.2792157.

Huber, L., Hadian, R., Grabowski, B., Neugebauer, J., 2018. A machine learning approach to model solute grain boundary segregation. npj Computational Materials, 4(1), p.64. https://doi.org/10.1038/s41524-018-0122-7.

Hunter, A., Moore, B.A., Mudunuru, M., Chau, V., Tchoua, R., Nyshadham, C., Karra, S., O'Malley, D., Rougier, E., Viswanathan, H., Srinivasan, G., 2019. Reduced-order modeling through machine learning and graph-theoretic approaches for brittle fracture applications. Computational Materials Science, 157, pp.87-98. https://doi.org/10.1016/j.commatsci.2018.10.036.

Hutchinson, J.W., Evans, A.G., 2000. Mechanics of materials: top-down approaches to fracture. Acta materialia, 48(1), pp.125-135. https://doi.org/10.1016/S1359-6454(99)00291-8.

Iman, M., Arabnia, H.R., Rasheed, K., 2023. A review of deep transfer learning and recent advancements. Technologies, 11(2), p.40. https://doi.org/10.3390/technologies11020040.

Kanir, T., N'Guyen, F., Forest, S., Jeulin, D., Reed, M., Singleton, S., 2006. Apparent and effective physical properties of heterogeneous materials: Representativity of samples of two materials from food industry. Computer Methods in Applied Mechanics and Enigneering, 195 (33-36), p. 3960-3982.

Keralavarma, S.M., Benzerga, A.A., 2010. A constitutive model for plastically anisotropic solids with non-spherical voids. Journal of the Mechanics and Physics of Solids, 58(6), pp.874-901. https://doi.org/10.1016/j.jmps.2010.03.007.

Kim, H.G., Chew, H.B., Kim, K.S., 2012. Inverse extraction of cohesive zone laws by field projection method using numerical auxiliary fields. International journal for numerical methods in engineering, 91(5), pp.516-530. https://doi.org/10.1002/nme.4281.

Koric, S., Abueidda, D.W., 2023. Data-driven and physics-informed deep learning operators for solution of heat conduction equation with parametric heat source. International Journal of Heat and Mass Transfer, 203, p.123809. https://doi.org/10.1016/j.ijheatmasstransfer.2022.123809.

Kozák, V., Vlček, L., 2005. Parameters identification for GTN model and their verification on 42CrMo4 steel. In Materials Science Forum (Vol. 482, pp. 335-338). Trans Tech Publications Ltd. https://doi.org/10.4028/www.scientific.net/MSF.482.335.

Lacroix, R., Leblond, J.B., Perrin, G., 2016. Numerical study and theoretical modelling of void growth in porous ductile materials subjected to cyclic loadings. European Journal of Mechanics-A/Solids, 55, pp.100-109. https://doi.org/10.1016/j.euromechsol.2015.08.010.

Lebensohn, R.A., Tomé, C.N., Maudlin, P.J., 2004. A selfconsistent formulation for the prediction of the anisotropic behavior of viscoplastic polycrystals with voids. Journal of the Mechanics and Physics of Solids, 52(2), pp.249-278. https://doi.org/10.1016/S0022-5096(03)00114-5.

Leblond, J.B., Perrin, G., Devaux, J., 1995. An improved Gurson-type model for hardenable ductile metals. European journal of mechanics. A. Solids, 14(4), pp.499-527. https://api.semanticscholar.org/CorpusID:118050919.

McClintok, F.A., 1968. A criterion for ductile fracture by growth of holes. Journal of Applied Mechanics, 35(4), pp.353-371. https://doi.org/10.1115/1.3601204.

Mear, M.E., Hutchinson, J.W., 1985. Influence of yield surface curvature on flow localization in dilatant plasticity. Mechanics of materials, 4(3-4), pp.395-407. https://doi.org/10.1016/0167-6636(85)90035-3.

Moayedi, H., Mosallanezhad, M., Rashid, A.S.A., Jusoh, W.A.W., Muazu, M.A., 2020. A systematic review and meta-analysis of artificial neural network application in geotechnical engineering: theory and applications. Neural Computing and Applications, 32, pp.495-518. https://doi.org/10.1007/s00521-019-04109-9.

Monchiet, V., Cazacu, O., Charkaluk, E., Kondo, D., 2008. Macroscopic yield criteria for plastic anisotropic materials containing spheroidal voids. International Journal of Plasticity, 24(7), pp.1158-1189. https://doi.org/10.1016/j.ijplas.2007.08.008.

Monchiet, V., Bonnet, G., 2013. A Gurson-type model accounting for void size effects. International Journal of Solids and Structures, 50(2), pp.320-327. https://doi.org/10.1016/j.ijsolstr.2012.09.005.

Moore, B.A., Rougier, E., O'Malley, D., Srinivasan, G., Hunter, A., Viswanathan, H., 2018. Predictive modeling of dynamic fracture growth in brittle materials with machine learning. Computational Materials Science, 148, pp.46-53. https://doi.org/10.1016/j.commatsci.2018.01.056.

Morin, L., Leblond, J.B., Kondo, D., 2015. A Gurson-type criterion for plastically anisotropic solids containing arbitrary ellipsoidal voids. International Journal of Solids and Structures, 77, pp.86-101. https://doi.org/10.1016/j.ijsolstr.2015.05.021.

Morin, L., Michel, J.C., Leblond, J.B., 2017. A Gurson-type layer model for ductile porous solids with isotropic and kinematic hardening. International Journal of Solids and Structures, 118, pp.167-178. https://doi.org/10.1016/j.ijsolstr.2017.03.028.

Muro-Barrios, R., Cui, Y., Lambros, J., Chew, H.B., 2022. Dual-scale porosity effects on crack growth in additively manufactured metals: 3D ductile fracture models. Journal of the Mechanics and Physics of Solids, 159, p.104727. https://doi.org/10.1016/j.jmps.2021.104727.

Noh, W., Chew, H.B., 2024. Dislocation Descriptors of Low and High Angle Grain Boundaries with Convolutional Neural Networks. Extreme Mechanics Letters, p.102138. https://doi.org/10.1016/j.eml.2024.102138.

Paermentier, B., Debruyne, D., Talemi, R., 2021. A machine learning based sensitivity analysis of the GTN damage parameters for dynamic fracture propagation in X70 pipeline steel. International Journal of Fracture, 227(1), pp.111-132. https://doi.org/10.1007/s10704-020-00499-3.

Panwisawas, C., Perumal, B., Ward, R.M., Turner, N., Turner, R.P., Brooks, J.W., Basoalto, H.C., 2017. Keyhole formation and thermal fluid flow-induced porosity during laser fusion welding in

titanium alloys: Experimental and modelling. Acta materialia, 126, pp.251-263. https://doi.org/10.1016/j.actamat.2016.12.062.

Pardoen, T., Hutchinson, J.W., 2000. An extended model for void growth and coalescence. Journal of the Mechanics and Physics of Solids, 48(12), pp.2467-2512. https://doi.org/10.1016/S0022-5096(00)00019-3.

Pardoen, T., Hutchinson, J.W., 2003. Micromechanics-based model for trends in toughness of ductile metals. Acta Materialia, 51(1), pp.133-148. https://doi.org/10.1016/S1359-6454(02)00386-5.

Perrin, G., Leblond, J.B., 2000. Accelerated void growth in porous ductile solids containing two populations of cavities. International Journal of Plasticity, 16(1), pp.91-120. https://doi.org/10.1016/S0749-6419(99)00049-2.

Pierson, K., Rahman, A., Spear, A.D., 2019. Predicting microstructure-sensitive fatigue-crack path in 3D using a machine learning framework. Jom, 71(8), pp.2680-2694. https://doi.org/10.1007/s11837-019-03572-y.

Ragab, A.R., 2004a. Application of an extended void growth model with strain hardening and void shape evolution to ductile fracture under axisymmetric tension. Engineering Fracture Mechanics, 71(11), pp.1515-1534. https://doi.org/10.1016/S0013-7944(03)00216-9.

Ragab, A.R., 2004b. A model for ductile fracture based on internal necking of spheroidal voids. Acta Materialia, 52(13), pp.3997-4009. https://doi.org/10.1016/j.actamat.2004.05.015.

Reimanis, I.E., Dalgleish, B.J., Brahy, M., Rühle, M., Evans, A.G., 1990. Effects of plasticity on the crack propagation resistance of a metal/ceramic interface. Acta metallurgica et materialia, 38(12), pp.2645-2652. https://doi.org/10.1016/0956-7151(90)90277-N.

Rice, J.R., Tracey, D.M., 1969. On the ductile enlargement of voids in triaxial stress fields∗. Journal of the Mechanics and Physics of Solids, 17(3), pp.201-217. https://doi.org/10.1016/0022-5096(69)90033-7.

Rosenblatt, F., 1958. The perceptron: a probabilistic model for information storage and organization in the brain. Psychological review, 65(6), p.386. https://doi.org/10.1037/h0042519.

Rovinelli, A., Sangid, M.D., Proudhon, H., Ludwig, W., 2018. Using machine learning and a data-driven approach to identify the small fatigue crack driving force in polycrystalline materials. npj Computational Materials, 4(1), p.35. https://doi.org/10.1038/s41524-018-0094-7.

Schmidhuber, J., 2015. Deep learning in neural networks: An overview. Neural networks, 61, pp.85-117. https://doi.org/10.1016/j.neunet.2014.09.003.

Shafaie, M., Khademi, M., Sarparast, M., Zhang, H., 2022. Modified GTN parameters calibration in additive manufacturing of Ti-6Al-4 V alloy: a hybrid ANN-PSO approach. The International Journal of Advanced Manufacturing Technology, 123(11), pp.4385-4398. https://doi.org/10.1007/s00170-022-10522-7.

Shen, W.Q., Cao, Y.J., Shao, J.F., Liu, Z.B., 2020. Prediction of plastic yield surface for porous materials by a machine learning approach. Materials Today Communications, 25, p.101477. https://doi.org/10.1016/j.mtcomm.2020.101477.

Shikalgar, T.D., Dutta, B.K., Chattopadhyay, J., 2020. Analysis of p-SPT specimens using Gurson parameters ascertained by Artificial Neural Network. Engineering Fracture Mechanics, 240, p.107324. https://doi.org/10.1016/j.engfracmech.2020.107324.

Smith, M., 2009. ABAQUS/standard user's manual, version 6.9.

Snow, Z., Nassar, A.R., Reutzel, E.W., 2020. Invited Review Article: Review of the formation and impact of flaws in powder bed fusion additive manufacturing. Additive Manufacturing, 36, p.101457. https://doi.org/10.1016/j.addma.2020.101457.

Springmann, M., Kuna, M., 2005. Identification of material parameters of the Gurson–Tvergaard–Needleman model by combined experimental and numerical techniques. Computational Materials Science, 33(4), pp.501-509. https://doi.org/10.1016/j.commatsci.2005.02.002.

Stone, R.V., Cox, T.B., Low, J.R., Psioda, J.A., 1985. Microstructural aspects of fracture by dimpled rupture. International Metals Reviews, 30(1), pp.157-180. https://doi.org/10.1179/imtr.1985.30.1.157.

Teng, B., Wang, W., Liu, Y., Yuan, S., 2014. Bursting prediction of hydroforming aluminium alloy tube based on Gurson-Tvergaard-Needleman damage model. Procedia Engineering, 81, pp.2211-2216. https://doi.org/10.1016/j.proeng.2014.10.310.

Tekoglu, C., Nielsen, K.L., 2019. Effect of damage-related microstructural parameters on plate tearing at steady state. European Journal of Mechanics-A/Solids, 77, p.103818. https://doi.org/10.1016/j.euromechsol.2019.103818.

Tran, H., Chew, H.B., 2022. Cohesive zone interpretations of phase-field fracture models. Journal of Applied Mechanics, 89(12), p.121005. https://doi.org/10.1115/1.4055660.

Tran, H., Gao, Y.F., Chew, H.B., 2022. An inverse method to reconstruct crack-tip cohesive zone laws for fatigue by numerical field projection. International Journal of Solids and Structures, 239, p.111435. https://doi.org/10.1016/j.ijsolstr.2022.111435.

Tvergaard, V., 1981. Influence of voids on shear band instabilities under plane strain conditions. International Journal of fracture, 17, pp.389-407. https://doi.org/10.1007/BF00036191.

Tvergaard, V., 1982. Material failure by void coalescence in localized shear bands. International journal of solids and structures, 18(8), pp.659-672. https://doi.org/10.1016/0020-7683(82)90046-4.

Tvergaard, V., Huang, Y., Hutchinson, J.W., 1992. Cavitation instabilities in a power hardening elastic-plastic solid. European Journal of Mechanics A/Solids 11, 215-231.

Tvergaard, V., Hutchinson, J.W., 1992. The relation between crack growth resistance and fracture process parameters in elastic-plastic solids. Journal of the Mechanics and Physics of Solids, 40(6), pp.1377-1397. https://doi.org/10.1016/0022-5096(92)90020-3.

Tvergaard, V., 1998. Interaction of very small voids with larger voids. International Journal of Solids and Structures, 35(30), pp.3989-4000. https://doi.org/10.1016/S0020-7683(97)00254-0.

Tvergaard, V., Hutchinson, J.W., 2002. Two mechanisms of ductile fracture: void by void growth versus multiple void interaction. International Journal of Solids and Structures, 39(13-14), pp.3581-3597. https://doi.org/10.1016/S0020-7683(02)00168-3.

Ueda, T., Helfen, L., Morgeneyer, T.F., 2014. In situ laminography study of three-dimensional individual void shape evolution at crack initiation and comparison with Gurson–Tvergaard–Needleman-type simulations. Acta materialia, 78, pp.254-270. https://doi.org/10.1016/j.actamat.2014.06.029.

VanSickle, R., Foehring, D., Chew, H.B., Lambros, J., 2020. Microstructure effects on fatigue crack growth in additively manufactured Ti–6Al–4V. Materials Science and Engineering: A, 795, p.139993. https://doi.org/10.1016/j.msea.2020.139993.

Valoroso, N., Fedele, R., 2010. Characterization of a cohesive-zone model describing damage and de-cohesion at bonded interfaces. Sensitivity analysis and mode-I parameter identification. International Journal of Solids and Structures, 47(13), pp.1666-1677. https://doi.org/10.1016/j.ijsolstr.2010.03.001.

Varias, A.G., Suo, Z., Shih, C.F., 1991. Ductile failure of a constrained metal foil. Journal of the Mechanics and Physics of Solids, 39(7), pp.963-986. https://doi.org/10.1016/0022-5096(91)90014-F.

Wang, H., Zhang, W., Sun, F., Zhang, W., 2017. A comparison study of machine learning based algorithms for fatigue crack growth calculation. Materials, 10(5), p.543. https://doi.org/10.3390/ma10050543.

Wang, Y., Oyen, D., Guo, W., Mehta, A., Scott, C.B., Panda, N., Fernández-Godino, M.G., Srinivasan, G., Yue, X., 2021. StressNet-Deep learning to predict stress with fracture propagation in brittle materials. Npj Materials Degradation, 5(1), p.6. https://doi.org/10.1038/s41529-021-00151-y.

Wang, S., Wang, H., Perdikaris, P., 2021. Learning the solution operator of parametric partial differential equations with physics-informed DeepONets. Science advances, 7(40), p.eabi8605. https://doi.org/10.1126/sciadv.abi8605.

Williams, J.G., Hadavinia, H., 2002. Analytical solutions for cohesive zone models. Journal of the Mechanics and Physics of Solids, 50(4), pp.809-825. https://doi.org/10.1016/S0022-5096(01)00095-3.

Worthington, M., Chew, H.B., 2023. Crack path predictions in heterogeneous media by machine learning. Journal of the Mechanics and Physics of Solids, 172, p.105188. https://doi.org/10.1016/j.jmps.2022.105188.

Xia, L., Shih, C.F., 1995. Ductile crack growth-I. A numerical study using computational cells with microstructurally-based length scales. Journal of the Mechanics and Physics of Solids, 43(2), pp.233-259. https://doi.org/10.1016/0022-5096(94)00064-C.

Yang, X., Guan, J., Ding, L., You, Z., Lee, V.C., Hasan, M.R.M., Cheng, X., 2021. Research and applications of artificial neural network in pavement engineering: a state-of-the-art review. Journal of Traffic and Transportation Engineering (English Edition), 8(6), pp.1000-1021. https://doi.org/10.1016/j.jtte.2021.03.005.

Zhang, G., Patuwo, B.E., Hu, M.Y., 1998. Forecasting with artificial neural networks:: The state of the art. International journal of forecasting, 14(1), pp.35-62. https://doi.org/10.1016/S0169-2070(97)00044-7.

Figure Captions

Figure 1: (**a**) Schematic of a $D \times D \times D$ representative volume element (RVE) containing an initially spherical void under plane strain boundary conditions, and subjected to combined shear and biaxial strain-controlled loading. (**b**) Finite element mesh of the undeformed and deformed RVE as viewed from cross-sectional cuts across $x_3 = D/2$ (top) and $x_2 = D/2$ (bottom). R_0: initial void radius; a, b, c: major, minor, out-of-plane half-axis. (**c**) Uniaxial stress-strain response of matrix materials Mat 1, 2, and 3.

Figure 2: Gurson model (symbols) versus FEM predictions (lines) under uniaxial stress state: Equivalent stress (**a**), mean stress (**b**), and void porosity (**c**) evolution with equivalent strain for various initial porosities f_0.

Figure 3: Gurson model (symbols) versus FEM predictions (lines) under combined biaxial tension and shear loading ($\alpha_1 = 3, \alpha_2 = 5$): Equivalent stress (**a**), mean stress (**b**), and void porosity (**c**) evolution with equivalent strain for various initial porosities f_0. Inset in (**c**) denotes close-up view of the porosity evolutions for higher f_0.

Figure 4: (**a**) Flow-chart of a user material model, using a series of artificial neural networks (ANNs) to predict and update the stiffness matrix/stress increment (ANN-1), porosity (ANN-2), and void shape evolution (major half-axis: ANN-3, minor half-axis: ANN-4, out-of-plane half-axis: ANN-5) of a porous RVE under incremental loadings. (**b**) Architecture of a typical ANN comprising of a common input layer connected to hidden and output layers.

Figure 5: Evolution of individual stress components for ANNs trained on increasing load sets (symbols) versus FEM predictions (lines) under combined biaxial tension and shear loading ($\alpha_1 = 3, \alpha_2 = 5$).

Figure 6: Evolution of current porosity for ANNs trained on increasing load sets (symbols) versus FEM predictions (lines) under combined biaxial tension and shear loading ($\alpha_1 = 3, \alpha_2 = 5$).

Figure 7: Effects of monotonic variation of α_1 (**a**) under biaxial tension loading ($\alpha_2 = 0$) on ANN (symbols) versus FEM predictions (lines) of the equivalent stress (**b**), mean stress (**c**), and porosity evolution (**d**) for $f_0 = 0.05$. *Black solid line, square symbol*: $\alpha_1 = 1$. *Black dashed line, triangle symbol*: $\alpha_1 = 6$. *Blue line, cross symbol*: α_1 varying monotonically from 1 to 6. *Red line, circle symbol*: α_1 varying monotonically from 6 to 1.

Figure 8: Effects of non-monotonic variation of α_1 (**a**) under biaxial tension loading ($\alpha_2 = 0$) on ANN (symbols) versus FEM predictions (lines) of the equivalent stress (**b**), mean stress (**c**), and porosity evolution (**d**) for $f_0 = 0.05$. *Black solid line, square symbol*: $\alpha_1 = 1$. *Black dashed line, triangle symbol*: $\alpha_1 = 6$. *Blue line, cross symbol*: α_1 varying from 1 to 6 to 1. *Red line, circle symbol*: α_1 varying from 6 to 1 to 6.

Figure 9: Effects of initial porosity on ANN (symbols) versus FEM predictions (lines) of the equivalent stress (**a**), mean stress (**b**), and porosity evolution (**c**) under combined biaxial tension and shear loading ($\alpha_1 = 3, \alpha_2 = 5$). The case for $f_0 = 0$ is excluded in the training dataset of the ANNs. *Red*: interpolated results. *Blue*: extrapolated results.

Figure 10: Effects of initial porosity on ANN (symbols) versus FEM predictions (lines) of the major (**a**), minor (**b**), and out-of-plane (**c**) half-axes of the deformed void shape under combined

biaxial tension and shear loading ($\alpha_1 = 3, \alpha_2 = 5$). The case for $f_0 = 0$ is excluded in the training dataset of the ANNs. *Red*: interpolated results. *Blue*: extrapolated results.

Figure 11: Effects of number of hidden layers of ANN-1 which are fine-tuned on load set 1+2 for Mat 2: ANN predictions (symbols) of the equivalent stress (**a**), mean stress (**b**), and porosity evolution (**c**) for $f_0 = 0.005$ under combined biaxial tension and shear loading ($\alpha_1 = 3, \alpha_2 = 5$). *Solid line*: FEM results. *Dashed line*: ANN results without transfer learning (TF).

Figure 12: Effects of number of hidden layers of ANN-1 which are fine-tuned on load set 1+2 for Mat 2: ANN predictions (symbols) of the equivalent stress (**a**), mean stress (**b**), and porosity evolution (**c**) for $f_0 = 0.15$ under combined biaxial tension and shear loading ($\alpha_1 = 3, \alpha_2 = 5$). *Solid line*: FEM results. *Dashed line*: ANN results without transfer learning (TF).

Figure 13: Effects of number of hidden layers of ANN-1 which are fine-tuned on load set 1 (blue) or load set 1+2 (black) for Mat 3: ANN predictions (symbols) of the equivalent stress (**a**), mean stress (**b**), and porosity evolution (**c**) for $f_0 = 0.005$ under combined biaxial tension and shear loading ($\alpha_1 = 3, \alpha_2 = 5$). *Solid line*: FEM results. *Dashed line*: ANN results without transfer learning (TF).

Figure 14: Effects of number of hidden layers of ANN-1 which are fine-tuned on load set 1 (blue) or load set 1+2 (black) for Mat 3: ANN predictions (symbols) of the equivalent stress (**a**), mean stress (**b**), and porosity evolution (**c**) for $f_0 = 0.15$ under combined biaxial tension and shear loading ($\alpha_1 = 3, \alpha_2 = 5$). *Solid line*: FEM results. *Dashed line*: ANN results without transfer learning (TF).

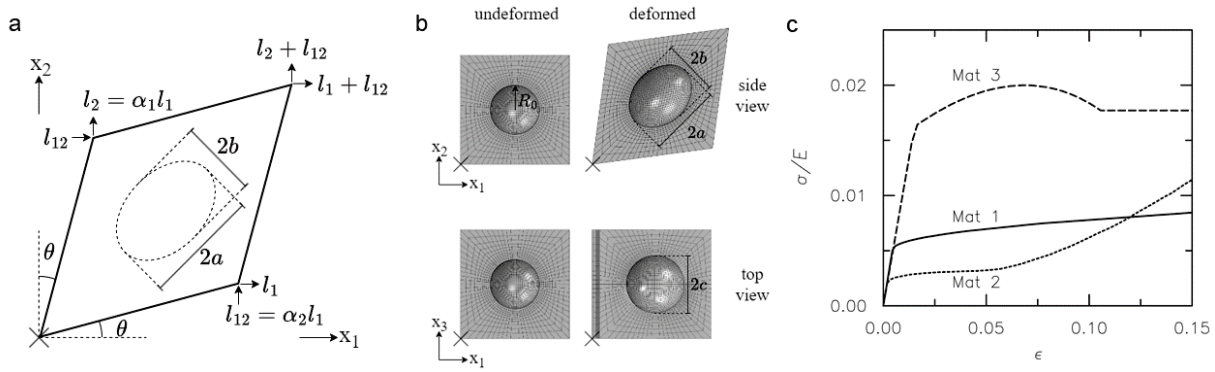

Figure 1: (**a**) Schematic of a $D \times D \times D$ representative volume element (RVE) containing an initially spherical void under plane strain boundary conditions, and subjected to combined shear and biaxial strain-controlled loading. (**b**) Finite element mesh of the undeformed and deformed RVE as viewed from cross-sectional cuts across $x_3 = D/2$ (top) and $x_2 = D/2$ (bottom). R_0: initial void radius; a, b, c: major, minor, out-of-plane half-axis. (**c**) Uniaxial stress-strain response of matrix materials Mat 1, 2, and 3.

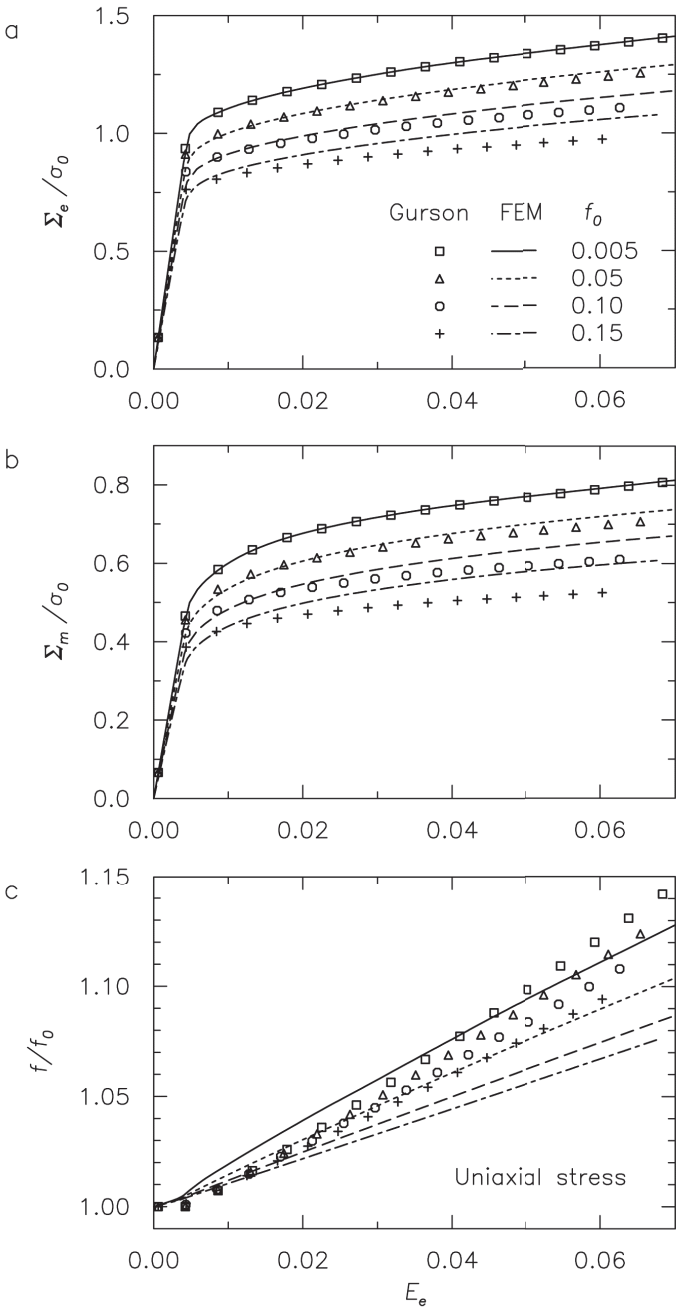

Figure 2: Gurson model (symbols) versus FEM predictions (lines) under uniaxial stress state: Equivalent stress (**a**), mean stress (**b**), and void porosity (**c**) evolution with equivalent strain for various initial porosities f_0.

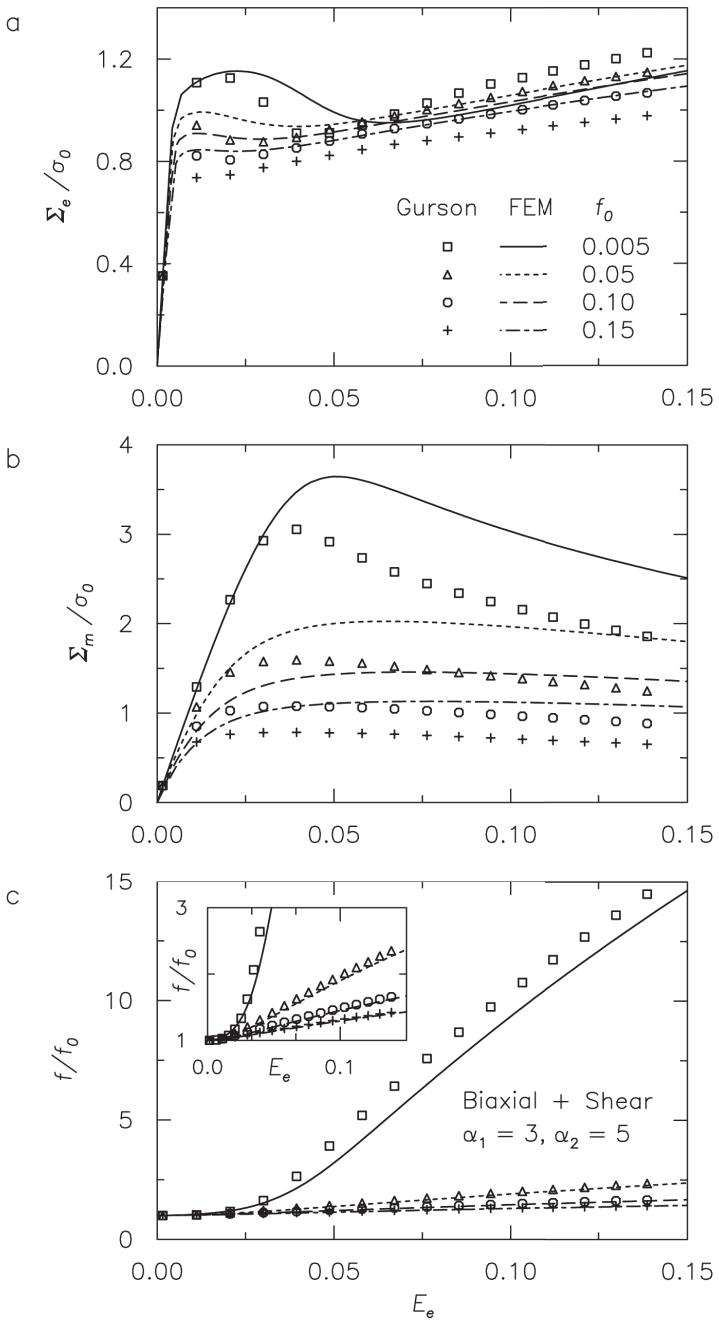

Figure 3: Gurson model (symbols) versus FEM predictions (lines) under combined biaxial tension and shear loading ($\alpha_1 = 3, \alpha_2 = 5$): Equivalent stress (**a**), mean stress (**b**), and void porosity (**c**) evolution with equivalent strain for various initial porosities f_0. Inset in (**c**) denotes close-up view of the porosity evolutions for higher f_0.

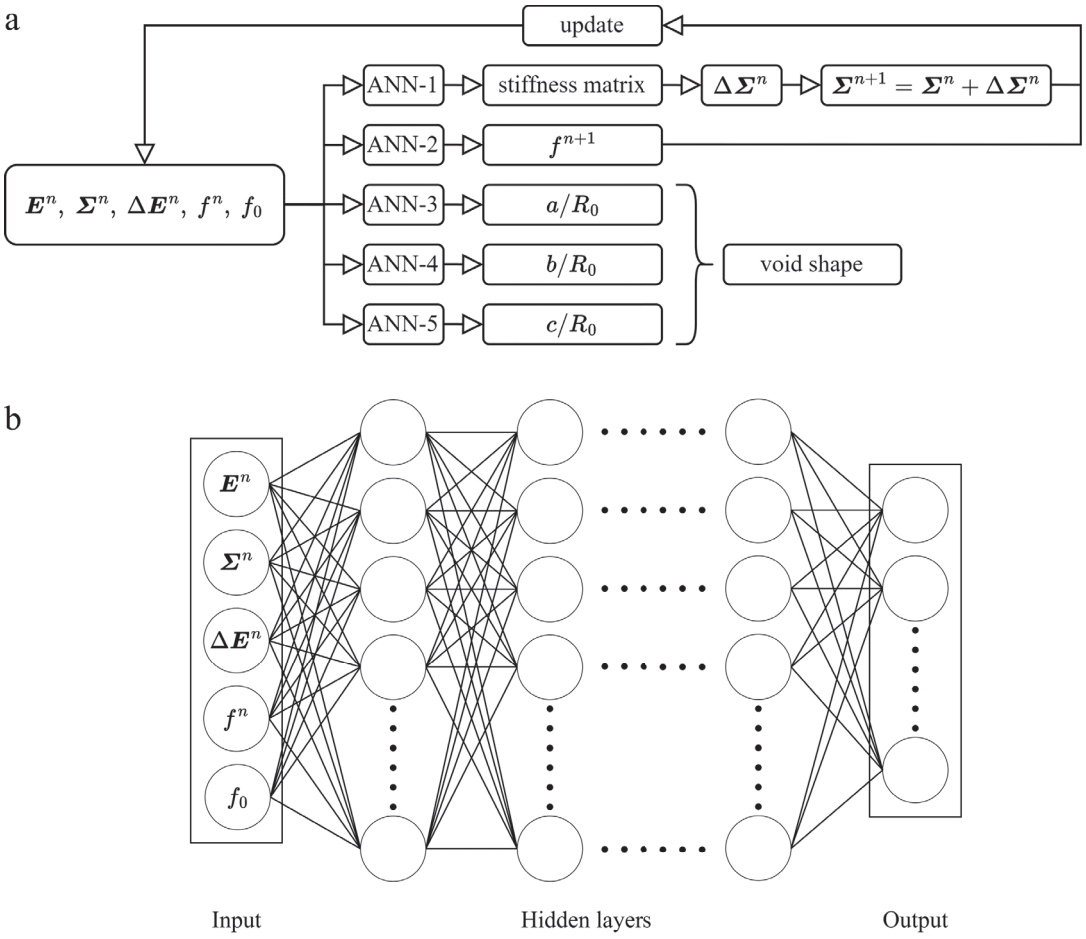

Figure 4: (**a**) Flow-chart of a user material model, using a series of artificial neural networks (ANNs) to predict and update the stiffness matrix/stress increment (ANN-1), porosity (ANN-2), and void shape evolution (major half-axis: ANN-3, minor half-axis: ANN-4, out-of-plane half-axis: ANN-5) of a porous RVE under incremental loadings. (**b**) Architecture of a typical ANN comprising of a common input layer connected to hidden and output layers.

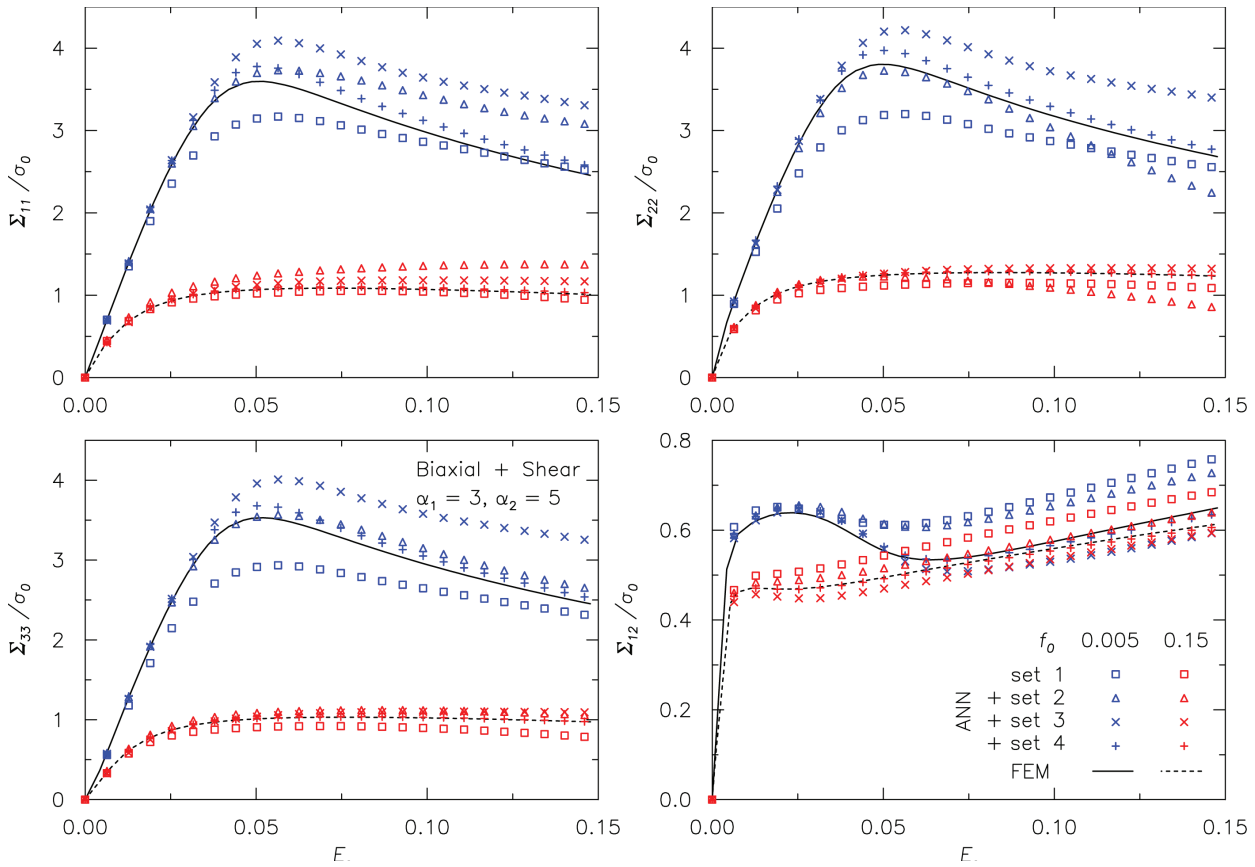

Figure 5: Evolution of individual stress components for ANNs trained on increasing load sets (symbols) versus FEM predictions (lines) under combined biaxial tension and shear loading ($\alpha_1 = 3, \alpha_2 = 5$).

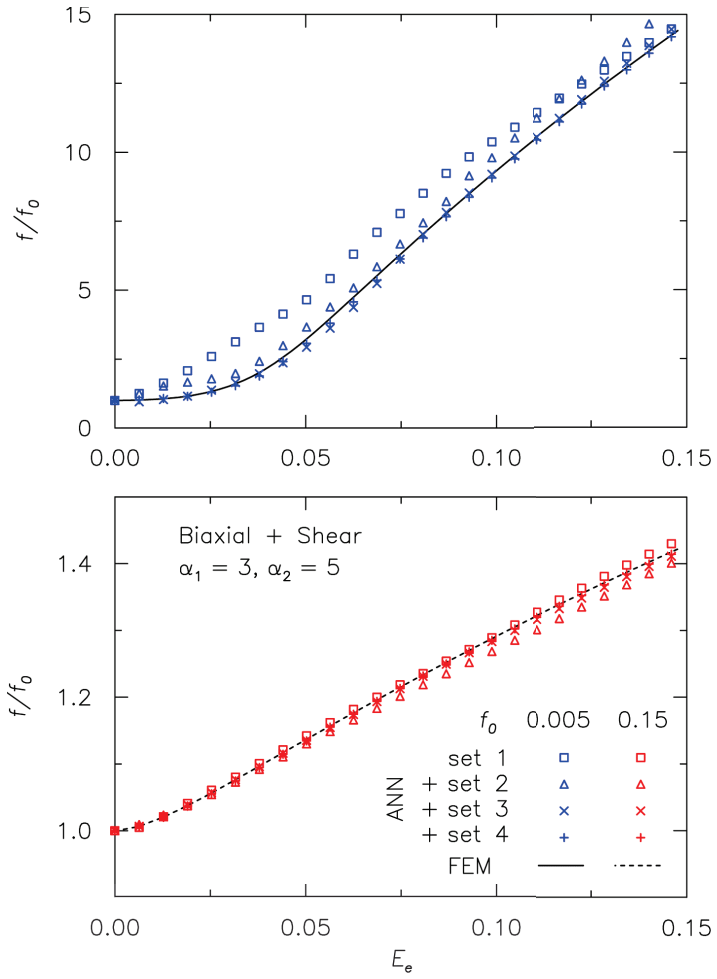

Figure 6: Evolution of current porosity for ANNs trained on increasing load sets (symbols) versus FEM predictions (lines) under combined biaxial tension and shear loading ($\alpha_1 = 3, \alpha_2 = 5$).

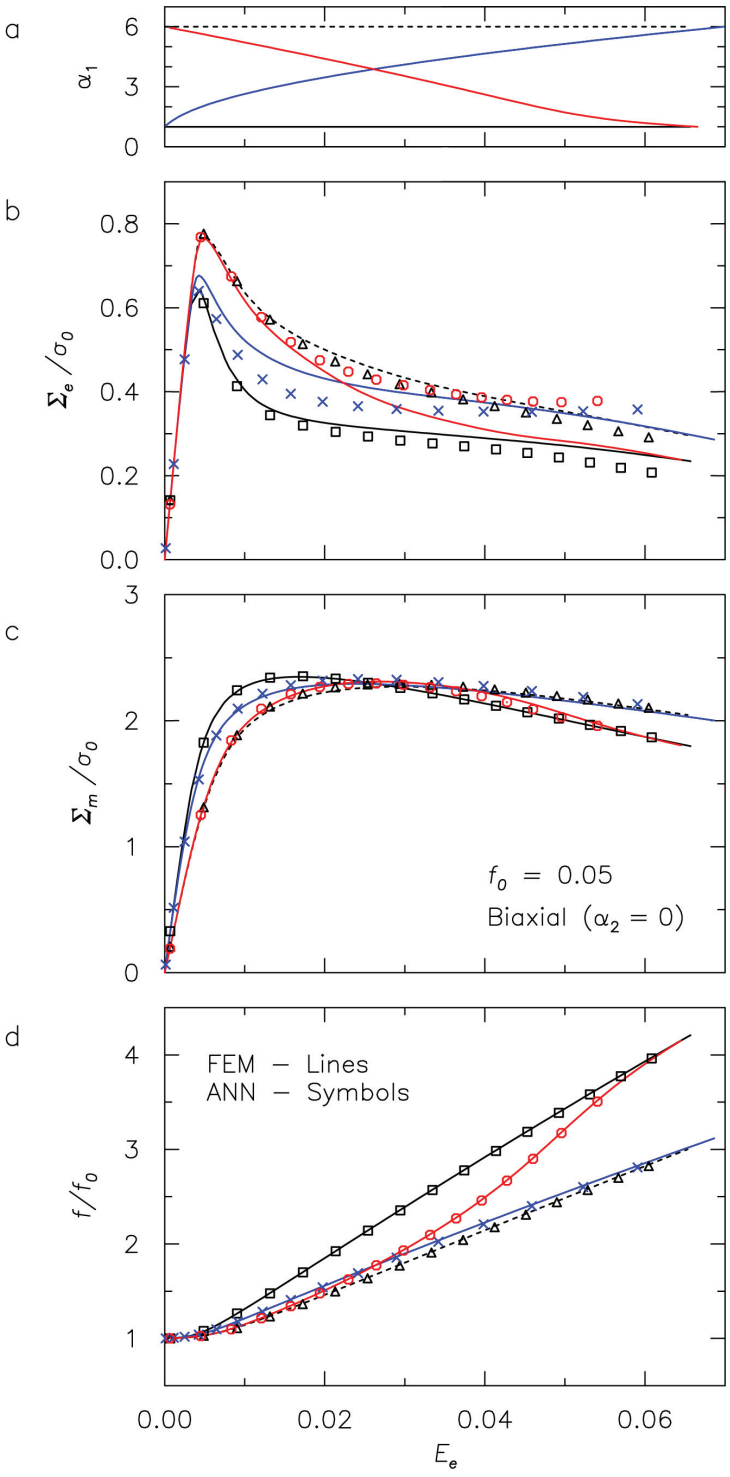

Figure 7: Effects of monotonic variation of α_1 (**a**) under biaxial tension loading ($\alpha_2 = 0$) on ANN (symbols) versus FEM predictions (lines) of the equivalent stress (**b**), mean stress (**c**), and porosity evolution (**d**) for $f_0 = 0.05$. *Black solid line, square symbol*: $\alpha_1 = 1$. *Black dashed line, triangle symbol*: $\alpha_1 = 6$. *Blue line, cross symbol*: α_1 varying monotonically from 1 to 6. *Red line, circle symbol*: α_1 varying monotonically from 6 to 1.

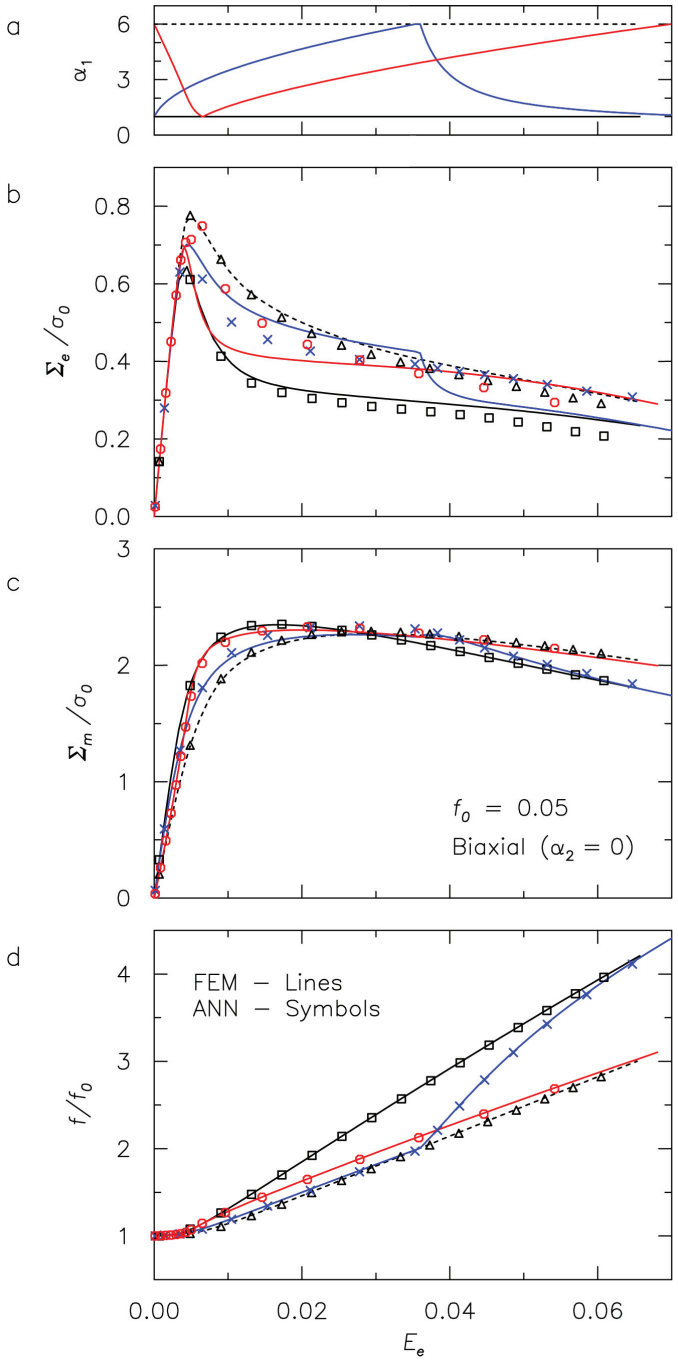

Figure 8: Effects of non-monotonic variation of α_1 (**a**) under biaxial tension loading ($\alpha_2 = 0$) on ANN (symbols) versus FEM predictions (lines) of the equivalent stress (**b**), mean stress (**c**), and porosity evolution (**d**) for $f_0 = 0.05$. *Black solid line, square symbol*: $\alpha_1 = 1$. *Black dashed line, triangle symbol*: $\alpha_1 = 6$. *Blue line, cross symbol*: α_1 varying from 1 to 6 to 1. *Red line, circle symbol*: α_1 varying from 6 to 1 to 6.

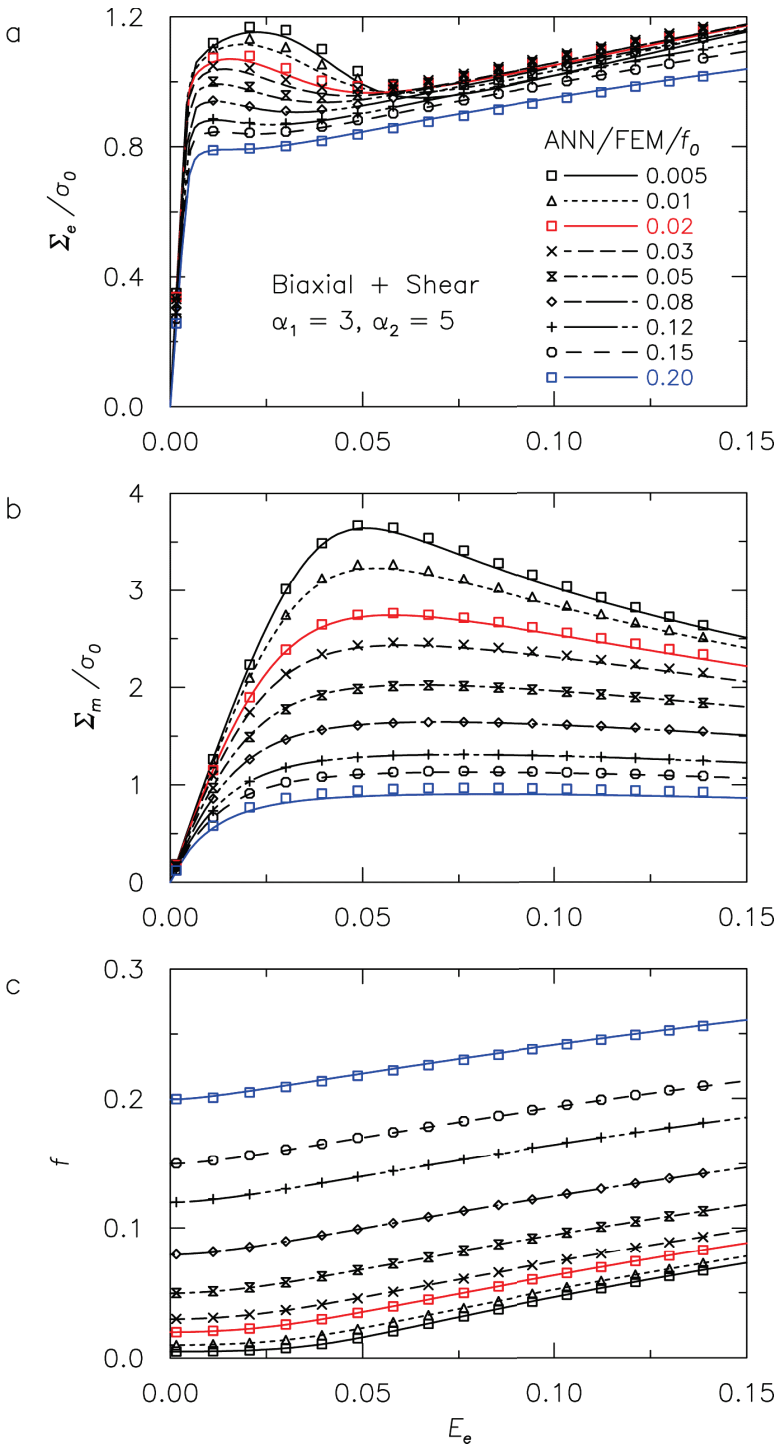

Figure 9: Effects of initial porosity on ANN (symbols) versus FEM predictions (lines) of the equivalent stress (**a**), mean stress (**b**), and porosity evolution (**c**) under combined biaxial tension and shear loading ($\alpha_1 = 3, \alpha_2 = 5$). The case for $f_0 = 0$ is excluded in the training dataset of the ANNs. *Red*: interpolated results. *Blue*: extrapolated results.

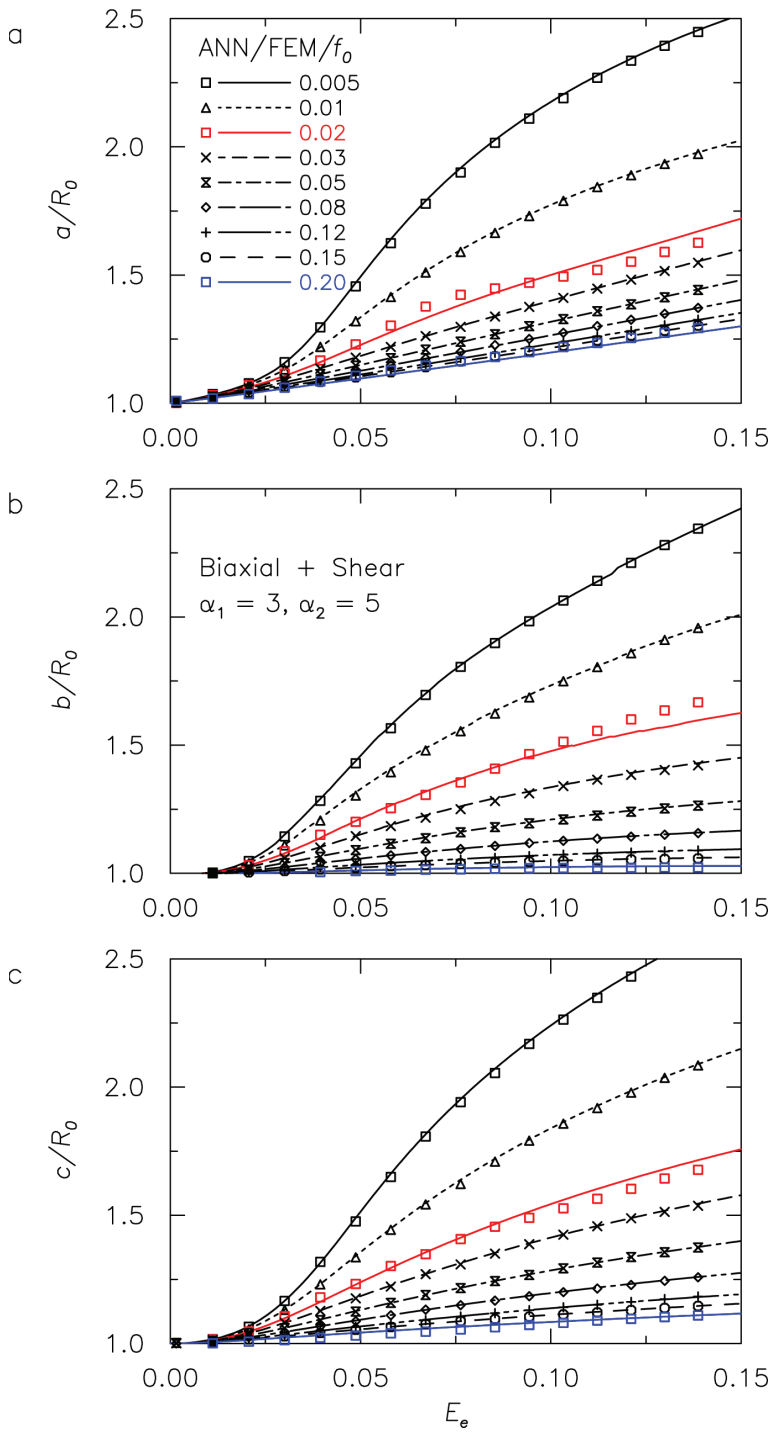

Figure 10: Effects of initial porosity on ANN (symbols) versus FEM predictions (lines) of the major (**a**), minor (**b**), and out-of-plane (**c**) half-axes of the deformed void shape under combined biaxial tension and shear loading ($\alpha_1 = 3, \alpha_2 = 5$). The case for $f_0 = 0$ is excluded in the training dataset of the ANNs. *Red*: interpolated results. *Blue*: extrapolated results.

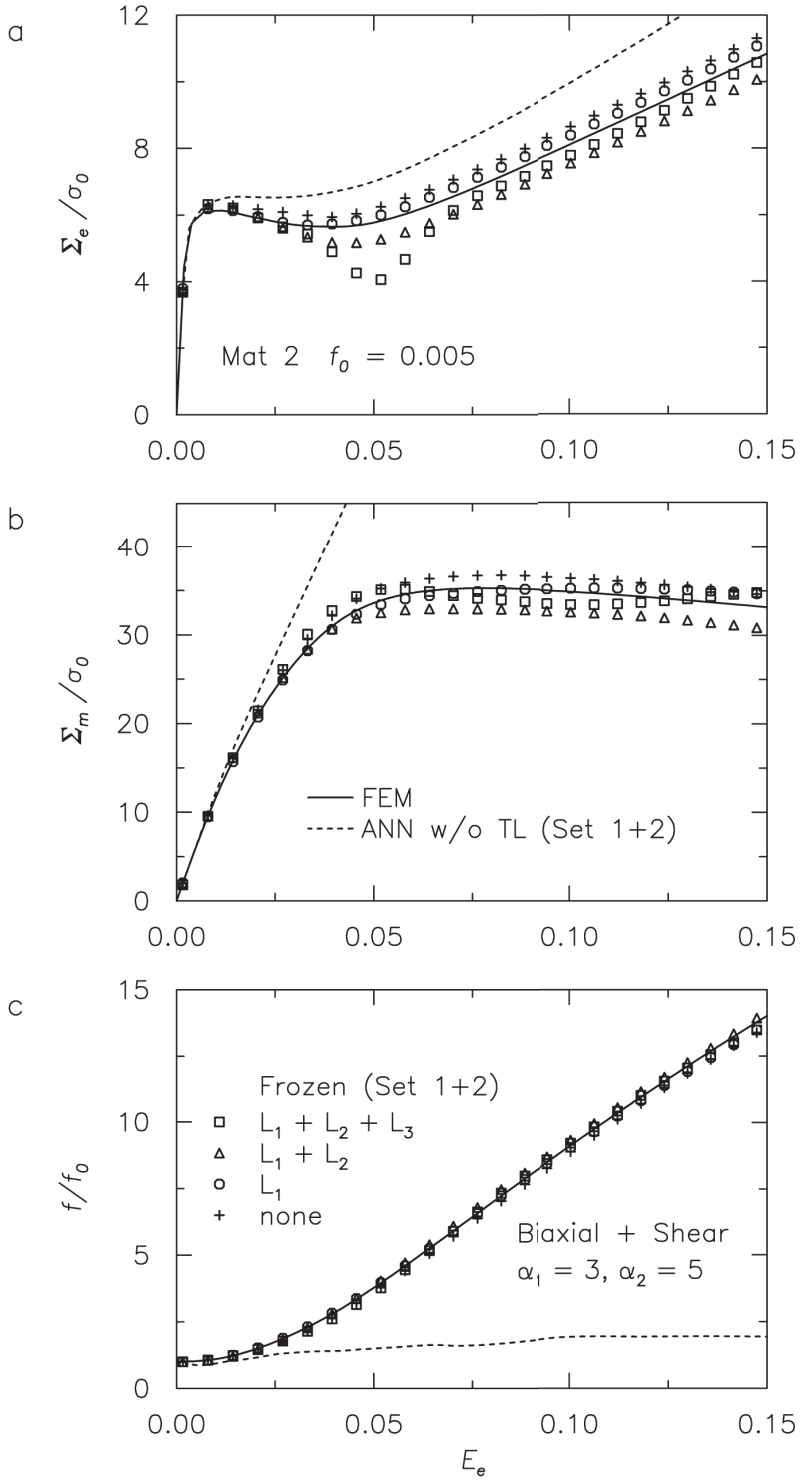

Figure 11: Effects of number of hidden layers of ANN-1 which are fine-tuned on load set 1+2 for Mat 2: ANN predictions (symbols) of the equivalent stress (**a**), mean stress (**b**), and porosity evolution (**c**) for $f_0 = 0.005$ under combined biaxial tension and shear loading ($\alpha_1 = 3, \alpha_2 = 5$). *Solid line*: FEM results. *Dashed line*: ANN results without transfer learning (TF).

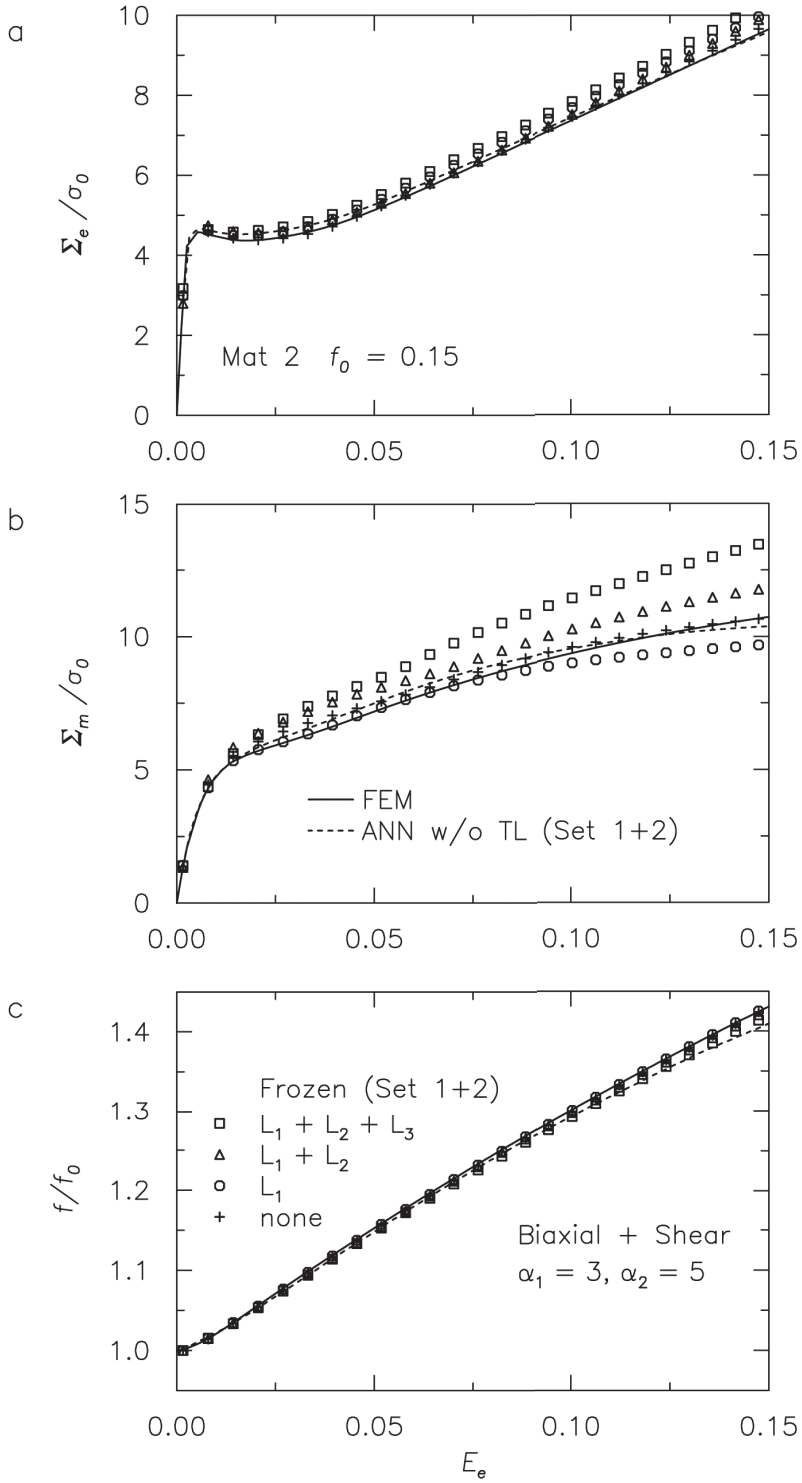

Figure 12: Effects of number of hidden layers of ANN-1 which are fine-tuned on load set 1+2 for Mat 2: ANN predictions (symbols) of the equivalent stress (**a**), mean stress (**b**), and porosity evolution (**c**) for $f_0 = 0.15$ under combined biaxial tension and shear loading ($\alpha_1 = 3, \alpha_2 = 5$). *Solid line*: FEM results. *Dashed line*: ANN results without transfer learning (TF).

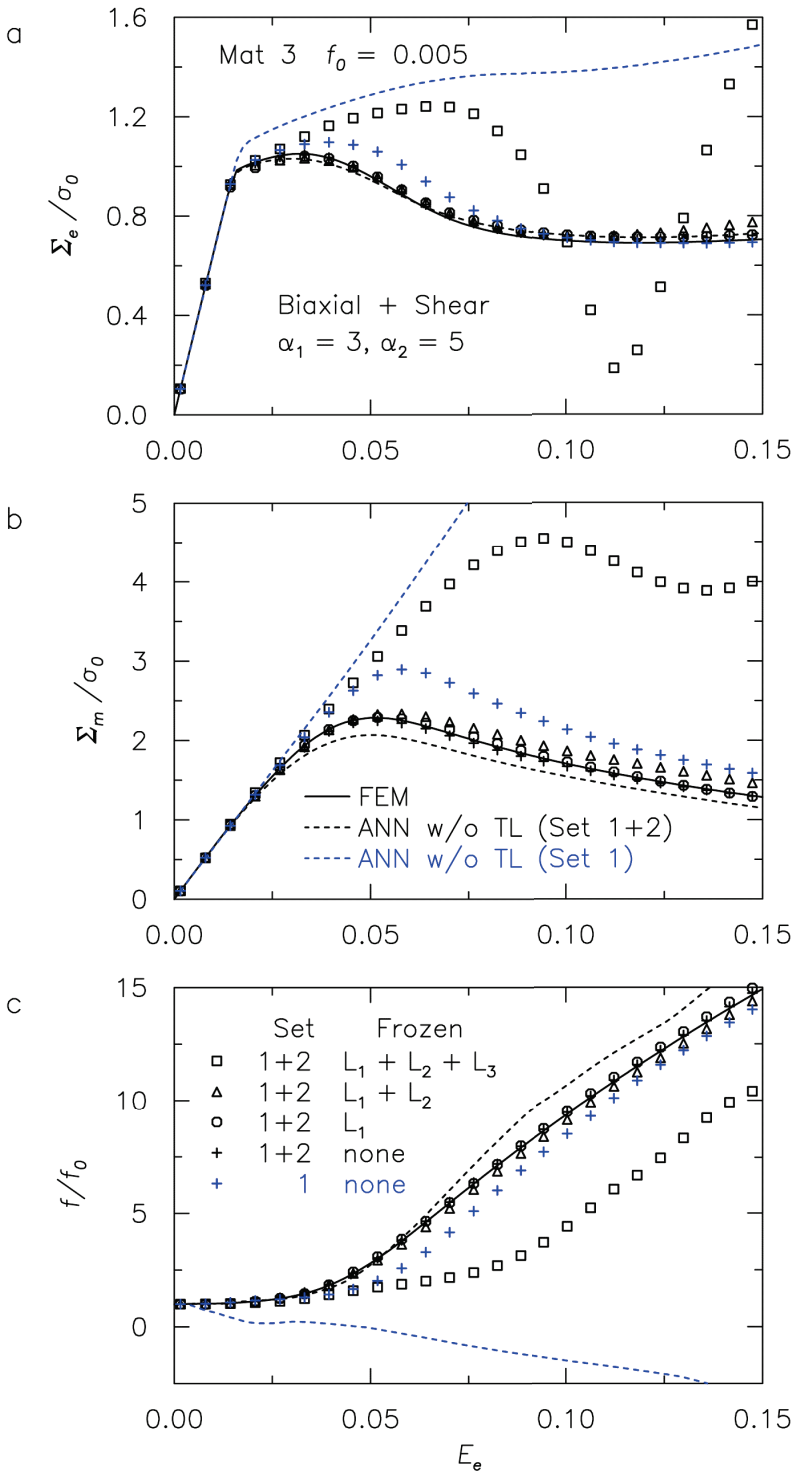

Figure 13: Effects of number of hidden layers of ANN-1 which are fine-tuned on load set 1 (blue) or load set 1+2 (black) for Mat 3: ANN predictions (symbols) of the equivalent stress (**a**), mean stress (**b**), and porosity evolution (**c**) for $f_0 = 0.005$ under combined biaxial tension and shear loading ($\alpha_1 = 3, \alpha_2 = 5$). *Solid line*: FEM results. *Dashed line*: ANN results without transfer learning (TF).

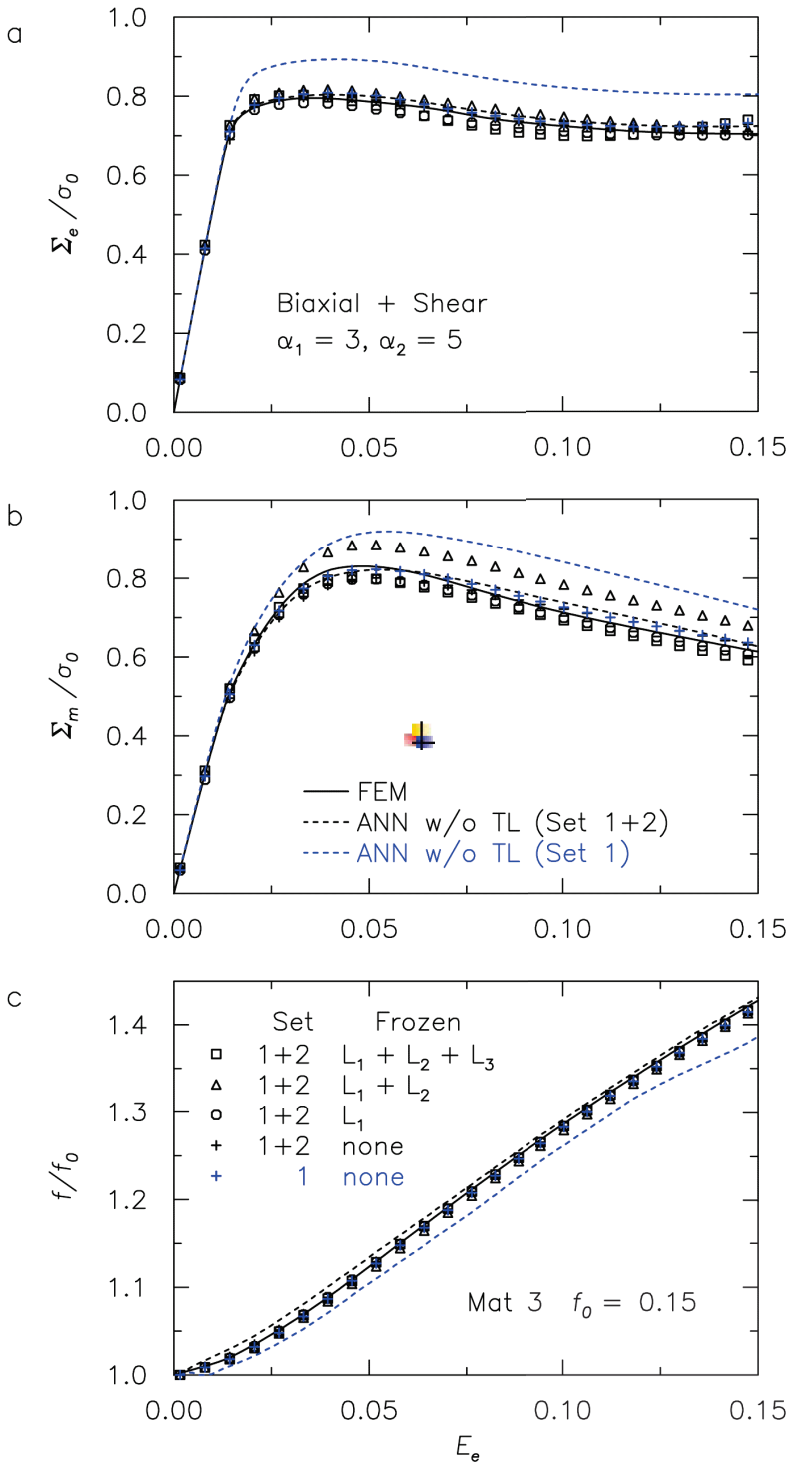

Figure 14: Effects of number of hidden layers of ANN-1 which are fine-tuned on load set 1 (blue) or load set 1+2 (black) for Mat 3: ANN predictions (symbols) of the equivalent stress (**a**), mean stress (**b**), and porosity evolution (**c**) for $f_0 = 0.15$ under combined biaxial tension and shear loading ($\alpha_1 = 3, \alpha_2 = 5$). *Solid line*: FEM results. *Dashed line*: ANN results without transfer learning (TF).